

國立交通大學

電信工程研究所

博士論文

長距離次載波/分波多工光纖系統與混合光纖同
軸擷取網路



Long-Distance DWDM/Subcarrier Multiplexed
Lightwave Systems and HFC Access Network
Architecture

研究生：陳威宏

指導教授：尉應時 教授

中華民國九十三年七月

長距離次載波/分波多工光纖系統與混合光纖
同軸擷取網路

Long-Distance DWDM/Subcarrier Multiplexed
Lightwave Systems and HFC Access Network
Architecture

研究生：陳威宏
指導教授：尉應時 教授

Student: Wei-Hung Chen
Advisor: Dr. Winston I. Way



A Dissertation
Submitted to the Institute of Communication Engineering
College of Electrical Engineering and Computer Science
National Chiao-Tung University
in
Partial Fulfillment of the Requirements
for the Degree of Doctor of Philosophy
in
Communication Engineering

July 2004
Hsinchu, Taiwan, Republic of China

中 華 民 國 九 十 三 年 七 月

長距離次載波/分波多工光纖系統與混合光纖 同軸擷取網路

研究生：陳威宏

指導教授：尉應時 教授

國立交通大學電信工程研究所

中 文 摘 要

在本論文中，我們研究將單頻帶/次載波 (SSB/SCM) 技術結合分波多工 (DWDM) 架構應用於都會型光網 (Metropolitan Optical Network) 的可行性。都會型光網不同一般長距離光纖通訊網路的特點在於：它要求高頻寬效益、高容量、高適應性（也就是說，每個次載波頻道裡的資料，彼此間是與通訊協定或資料速率無關的。）、且低成本。為了了解此系統在傳輸上的限制，我們在論文中推導出，由於 (1) Mach-Zehnder 光調變器與 (2) 光纖色散所導致的二階和三階拍差失真 (CSO、CTB) 的理論公式。另為了與分波多工的架構相結合，我們也同時推導在分波多工的架構下，由於光纖非線性所導致之物理現象 (Cross-Phase Modulation) 因而產生的光波長間干擾 (Crosstalk) 的理論與數值分析上的結果。此理論與數值分析並不受限於光波長間距的寬窄、每波長入射光的功率大小、調變訊號頻率的高低乃至光訊號的調變方式。以上所有的理論與數值分析結果都經由電腦模擬予以一一驗證。我們亦實際討論了兩個 SSB/SCM/DWDM 的系統以了解它們各自的基本限制與未來衍生的研究方向。

在本論文中，為了提供窄頻服務到用戶端，我們也提出了一個全新的，具有漸進式演化發展特性的混合光纖與同軸 (HFC) 擷取網路的架構，並以實驗驗證了它的可行性。此架構在演化的最初期並不要求一開始就鋪設昂貴的分波多工的許多主被動元件，例如 ITU 規格的雷射、分波多工器與解分波多工器等等。雖然如此，然而當每個光節點用戶的頻寬要求持續增加時，它卻也可以逐漸升等為多波長的分波多工架構。此外，此架構的特點是每個波長均可載多個次載波頻道以滿足節點用戶高容量的要求。

Long-Distance DWDM/Subcarrier Multiplexed Lightwave Systems and HFC Access Network Architecture

Student: Wei-Hung Chen

Advisor: Dr. Winston I. Way

Institute of Communication Engineering, National Chiao-Tung University

Abstract

In this dissertation, we investigate the applicability of single-sideband subcarrier-multiplexed (SSB/SCM) technology combined with dense wavelength-division-multiplexing (DWDM) scheme in the metropolitan optical network, which requires significantly more bandwidth-efficiency and high capacity with high granularity (protocol-and rate-independent at the same time) at low cost. To understand the transmission limitation of the SSB/SCM signals, we present a close-form analysis to predict the Mach-Zehnder intensity (MZI) modulator-induced composite triple beat (CTB), and linear-fiber-dispersion-induced composite second-order (CSO) and CTB distortions. To combine SSB/SCM with DWDM systems, analytical and numerical tools, which are not constrained by any wavelength spacing and modulation frequencies, are used to analyze cross-phase modulation (XPM) -induced crosstalk. All the analytical and numerical results are verified by computer simulations. Several multichannel SSB/SCM/DWDM systems with transport capacities of 10 or 20 Gb/s per wavelength, with a wavelength spacing of 25,50,100 GHz, are also studied in this dissertation to understand the fundamental transmission limitations.

We also proposed an evolutionary hybrid-fiber-coax (HFC) network architecture, which does not require DWDM in the beginning stage of adding narrowcast services, yet can be eventually upgraded using multiple DWDM wavelengths with a large channel loading per wavelength, is proposed and experimentally verified.

誌 謝

能夠順利畢業，最要感謝的是 尉應時 教授。尉老師不但在學術研究上具有先知卓見，指引我們正確而前瞻的研究方向；而老師嚴謹治學的態度，也使得我個人所獲甚多，使我們實驗室的研究成果，可以毫不畏懼地站上世界舞台，與全世界首屈一指的頂級實驗室分庭抗禮。這些參加大型國際學術會議的經驗，對於在台灣求學的我來說，實在是非常寶貴的學習機會。而在待人處世方面，老師更是以身作則，身教重於言教，對我們後輩有很深的啟發。此外，老師與師母對於我們，乃至於推己及人地，對於我們家人的貼心關懷與關心，亦使我銘記在心。



同時也要感謝祁甡教授、高銘盛教授、陳智弘助理教授、馮開明助理教授、張清添教授與王惠民學長等口試委員的不吝指正。尤其是高銘盛老師，不但在學術研究上常常給我新的啟發，且在我遇到問題與困難時，適時地給予鼓勵並提供我一個澄清的人生方向，繁此種種都令我深為感動。而在實驗室八年當中，能與實驗室的學長、學弟妹們共同研究、互相扶持、一起生活則將會是我永遠難以忘懷的愉快回憶。同樣地，曾同我走過這一階段的交大學弟妹們與朋友們，不論以後如何地物換星移，我亦會永遠記得發生在我們之間的點點滴滴。

最後，我要深深感謝這一路陪我走過來的家人—爸爸、媽媽、姊姊和最最最可愛的外甥們—怡慧和冠穎。謝謝你們的支持與陪伴！

Table of Contents

中 文 摘 要.....	i
Abstract.....	ii
誌 謝.....	iii
Table of Contents	iv
List of Tables.....	vi
List of Figures	vii
Chapter 1 Introduction (Overview)	1
1.1 Metropolitan Network.....	1
1.2 Why using Subcarrier Multiplexing (SCM)?.....	1
Chapter 2 Multi-Channel Single-Sideband SCM/DWDM Transmission Systems	4
2.1 System Configuration.....	5
2.2 Nonlinear Distortions in an SSB/SCM Transmission System — Single Subcarrier Channel.....	6
2.3 Nonlinear Distortions in an SSB/SCM Transmission System — Multiple Subcarrier Channels.....	11
2.4 SPM-Induced Impairment.....	18
2.5 DWDM Configuration – XPM Limitations.....	19
2.6 Complete System Performance Considering All Transmission Impairments..	30
2.7 Summary	36
Chapter 3 An Evolutionary HFC Network Architecture for Adding Narrowcast Services	39
3.1 Architectural Concept	40
3.2 Experiment and Analysis	41
3.3 Summary	44
Chapter 4 Conclusions.....	45

References.....	47
Tables	50
Figures.....	55
Publication List	76
簡 歷.....	77



List of Tables

Table 2.1	Analytic expressions for the individual third order distortions due to SSB/SCM Modulation, Ω_i , Ω_j and Ω_k , are three arbitrarily chosen distinct subcarrier frequencies.	50
Table 2.2	Analytic expressions for SSB/SCM 2 nd order NLDs due to linear fiber dispersion. $\rho = 1/2 \cdot \beta_2 \cdot z$	51
Table 2.3	Parameters for a 20 Gb/s SSB/SCM systems	52
Table 2.4	For the system given in Table 2.3, a summary of the optimum optical power, <i>RMS OMI/ch</i> and the corresponding worst-case NSR in a transmission system with four multiplexed wavelengths. Three wavelength spacings are given: 25, 50 and 100 GHz. The required coding gains to reach a BER of 10^{-12} are also shown.	53
Table 2.5	For 32 channels of 16-QAM signals equally distributed between 6.882 and 12.648 GHz (same transport capacity as that given in Table 2.3), a summary of the optimum optical power, RMS OMI/ch and the corresponding worst-case NSR in a transmission system with four multiplexed wavelengths. Three wavelength spacings are studied: 25, 50 and 100 GHz. The required coding gains to reach a BER of 10^{-12} for QPSK and 16-QAM are also shown.	54

List of Figures

Fig. 2.1	An SSB/SCM/DWDM system.....	55
Fig. 2.2	Optical spectrum of a single channel SSB/SCM signal with $m=0.1$ (note that ω_0 is subtracted from all frequency components).	56
Fig. 2.3	Optical spectrum of a 2-ch SSB/SCM signal with $m=0.1$ (note that ω_0 is subtracted from all frequency components).....	57
Fig. 2.4	Noise-to-signal ratio (NSR) versus frequency in an SSB/SCM optical transmission system with 64 QPSK channels (ranging from 0.93 to 12.648 GHz), for fiber lengths of 0 and 80 km. Dashed line and upper triangular symbols are the theoretical and simulation results for the case of no fiber transmission, respectively. Solid lines and circular symbols are the theoretical and simulation results after 80 km fiber transmission, respectively. RMS OMI per channel is around 4%.....	58
Fig. 2.5	Linear fiber dispersion-induced CSO versus transmission distance in a SSB/SCM system with 64 QPSK channels. Dashed and solid lines are the results of channel 32 and worst-case channel, respectively. RMS OMI per channel is 4%.....	59
Fig. 2.6	Noise-to-signal ratio (NSR) versus frequency in an SSB/SCM optical transmission system with 32 16-QAM channels (ranged from 6.882 to 12.648 GHz), for fiber lengths of 0, 30 and 80 km. Dashed line and upper triangular symbols are the theoretical and simulation results for the case of no fiber transmission, respectively. Square and circle symbols are the simulation results after 30 and 80km fiber transmissions, respectively. Solid lines are the	

theoretical results. RMS OMI per channel is around 1.8%.....	60
Fig. 2.7 Linear fiber dispersion-induced CTB versus transmission distance in an SSB/SCM system with 32 16-QAM channels. Dashed and solid lines are the results of channel 16 and worst-case channel, respectively. Dotted line is the intrinsic MZI-induced CTB at channel 16. RMS OMI per channel is 1.8%.....	61
Fig. 2.8 Two wavelengths XT versus pump modulation frequency for an average optical power per wavelength of 0, 6 or 10 dBm. Circular ($\Delta\lambda_{bp} = -0.2$ nm) and triangular ($\Delta\lambda_{bp} = +0.2$ nm) symbols are simulation results; dashed ($\Theta_p = 0$) and dotted ($\Theta_p \neq 0$) lines show the theoretical predictions; solid lines are numerical results. The pump wave is modulated with 64 QPSK channels between 0.93 and 12.648 GHz using USB/SCM.....	62
Fig. 2.9 Four wavelengths XT versus pump modulation frequency for wavelength separations of 25, 50 and 100 GHz (with the probe channel in the center (λ_3)). Circular, dotted and solid lines show the simulation, theoretical and numerical results, respectively. Three pump wavelengths are simultaneously modulated by three uncorrelated 64 QPSK channels (between 0.93 and 12.648 GHz) using USB/SCM. The average optical power per wavelength is 6 dBm.....	63
Fig. 2.10 Theoretical results of the worst channel NSR versus the <i>RMS OMI/ch</i> for an average optical power per wavelength of -2, 4 and 10 dBm, for the system given in Table 2.3. Dotted lines are for single wavelength, while solid lines are for four wavelengths. The wavelength separation is 50 GHz. Dashed line is due to linear fiber dispersion-induced CSO.....	64
Fig. 2.11 NSR versus channel frequency in the case of four wavelengths for the system	

given in Table 2.3. Average optical power per wavelength is -2, 4 or 10 dBm. Circular symbols are simulation results; dotted lines are theoretical results; and solid lines are numerical results. The wavelength separation is 50 GHz and RMS OMI per channel is 1.8%.....	65
Fig. 2.12 Theoretical results of the worst channel NSR versus the <i>RMS OMI/ch</i> for an average optical power per wavelength of -6, 0 and 6 dBm. Dotted lines are for the case of single wavelength, while solid lines are for the case of four wavelengths. The wavelength separation is 50 GHz. Dashed line is due to linear fiber dispersion-induced CTB.....	66
Fig. 2.13 NSR versus the channel frequency in the case of four wavelengths. Average optical power per wavelength is -6, 0 or 6 dBm. Circular symbols are simulation results; dotted lines are theoretical results; and solid lines are numerical results. The wavelength separation is 50 GHz and RMS OMI per channel is 5.5%.....	67
Fig. 3.1 Proposed HFC Network architecture for adding narrowcast services to broadcast services.....	68
Fig. 3.2 Measured SBS threshold versus <i>OMI/ch</i> for 81 km conventional SMF.....	69
Fig. 3.3 Measured C/CTB (●) and C/(CTB+N) (■) of Ch.50 (centered@ $f = 745.25$ MHz, Bandwidth = 6 MHz) versus <i>OMI/ch</i> . Dashed and solid lines are analytical results.....	70
Fig. 3.4 Received RF spectrum after 102.5 km conventional SMF transmission and 14 dB splitting loss.....	71
Fig. 3.5 C/CTB (●) and C/(CTB+N) (■) as a function of channel frequency. The	

dashed and solid lines are analytical results.....	72
Fig. 3.6 4-wavelength experimental setup for measuring DWDM crosstalk. Wavelength spacing was 3.2 nm.....	73
Fig. 3.7 Measured crosstalk in the probe wavelength due to λ_1 (∇), λ_2 (\blacksquare), λ_3 (\blacktriangle) and total crosstalk (\bullet) as a function of channel frequency. All broken lines are analytical results. Solid line is the predicted crosstalk at the middle (worst case) wavelength. Transmission distance is 80 km.....	74
Fig. 3.8 Predicted maximum transmission distance between primary and secondary hub versus wavelength spacing for 4 (\blacksquare), 8 (\bullet) and 16 (\blacktriangle) wavelengths. The transmission distance between secondary hub and optical nodes is fixed at 20 km.....	75



Chapter 1 Introduction (Overview)

1.1 Metropolitan Network

Metropolitan optical networks are characterized by densely populated areas, a large number of central offices, short distances between these interconnecting central offices, and lower data rates than long distance networks (typically less than 2.5 Gbps). In metropolitan networks, the traffic patterns change rapidly and require dynamic interconnections at these numerous central offices.

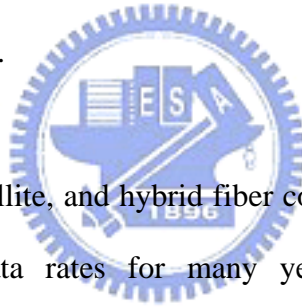
Capacity constraints in metropolitan optical networks are becoming frequent and common as data transmission consumes all available metropolitan fiber optical bandwidth. Capacity demand is being driven principally by the growth of the Internet, home office usage, e-commerce, and other broadband services. Moreover, enterprises that currently access the WAN through T1 circuits will require DS-3 and OC-3 connections in the near future in order to support virtual private networks and high-speed Internet access. Heavy and unpredictable data traffic, a condition present in many metropolitan areas, is driving an intense need for a metropolitan network solution that will optimize the installed fiber infrastructure and provide flexible capacity cost-effectively.

1.2 Why using Subcarrier Multiplexing (SCM)?

Demand for more flexible capacity creation at lower cost is causing service providers to look at alternative and complementary technologies to traditional time division multiplexing (TDM) systems. Subcarrier multiplexing (SCM) provides an additional dimension of multiplexing to increase the bandwidth-efficiency, overall capacity, and flexibility of optical

transport networks.

TDM is the other technology usually employed to increase capacity in metropolitan networks. TDM equipment offers flexible add/drop multiplexing, remote management, and performance monitoring. However, TDM solutions do not offer the level of granularity required on the tributary inputs and outputs. In order to serve the OC-3 or lower speed services required in the metropolitan market, OC-192 systems require external multiplexers, which adds cost and consumes valuable space. Higher data rate TDM is therefore not cost-effective in many metropolitan applications. Furthermore, TDM system is not particularly scalable, since the common equipment high-speed components represent high first cost. Finally, TDM does not offer the protocol and data rate independence obtained with DWDM technology.



SCM has been used in radio, satellite, and hybrid fiber coax (cable-TV, cable-modem, etc.) applications at much lower data rates for many years, providing low-cost, highly bandwidth-efficient physical-layer transport. SCM is a scheme where multiple bandwidth-efficient modulated signals, translating to lower speed (and cost) electronics and to an ability to transmit more information in a given bandwidth, are multiplexed in the radio-frequency (RF) domain and transmitted by a single wavelength. For optical modulation, a scheme of optical single sideband (OSSB) is used to eliminate the need for chromatic dispersion compensation in all but long-distance optical networks. Such an SCM system described above achieves the features desired for metropolitan networks. It provides significantly more bandwidth-efficiency and high capacity with high granularity at low cost. Significantly more bandwidth-efficiency and high capacity are attributed to the combined technologies of SCM and OSSB in the system. Low cost is achieved by using commercially available, standard components developed and proved for other high-volume

industries. In the meanwhile, multiple advanced Forward-error-correction (FEC) coding algorithms were exploited so that performance comparable to or better than alternative approaches can be achieved with similar power. The SCM channels can be protocol-independent and rate-independent, since no synchronization is required among the channels. Finally, SCM can be combined with TDM on the tributaries and DWDM on the high-speed side to achieve even greater granularity and higher overall capacity.



Chapter 2 Multi-Channel Single-Sideband SCM/DWDM Transmission Systems

In a conventional SCM transmission system, lower and upper subcarrier sidebands appear on both sides of an optical carrier, and their phases tend to rotate with respect to each other due to the chromatic dispersion in a standard single-mode fiber (SMF). At a certain transmission distance, the two sidebands could be 180° out of phase, and after down-conversion through a square-law photo-detector, the signal is cancelled out. This kind of “fading” phenomenon could periodically occur at different transmission distances along a fiber link. Single sideband SCM (SSB/SCM) modulation eliminates the energy on one side of the optical carrier, and consequently its chromatic dispersion tolerance is significantly enhanced – limited only by the symbol rate of the individual subcarriers not by the aggregate signal bandwidth while an optical filter before the photodiode is adopted to select a certain sub-channel; or the usage of the bandwidth is not limited any more by the first-order RF power degradation while utilizing broadband detection at the receiver end. As a result, SSB/SCM has been used in wireless-optical fiber links operating at millimeter-wave subcarriers to carry a narrowband signal, such as 51.8 Mb/s at 12 GHz over 80 km of SMF [1], and 155 Mb/s at 38 GHz over 50 km of SMF [2]. SSB/SCM has also been applied to a transmission system carrying multiple channels, for example, a system with 70 channels of 6 MHz AM-VSB at 28 GHz over 23.8 km of SMF was studied [3]. However, only simulation results were provided in [3], and no clear analytical guideline was given.

In this chapter, we first study the fundamental transmission limitations in a single wavelength, multi-channel SSB/SCM system. These include fiber dispersion-induced

second- and third-order nonlinear distortions, and the effect of self-phase modulation (SPM). We then investigate whether DWDM can be used in combination with multi-channel SSB/SCM modulation technique. Computer simulations, numerical calculations, and fundamental analytical tools are provided to understand the effect of cross-phase modulation (XPM) [4] and XPM-to-IM conversion via group velocity dispersion, for various wavelength spacing and modulation frequencies. We also present a few metro optical network case studies to understand the applicability of SSB/SCM/DWDM. Our fundamental analysis and numerical calculations can be easily extended to multi-channel wireless-optical fiber links.

2.1 System Configuration

Fig. 2.1 illustrates the basic SSB/SCM/DWDM system configuration. Multiple SCM channels from digital modems at a single intermediate frequency, with or without FEC codecs, are frequency converted and filtered to a series of equally spaced subcarrier frequencies (f_1, f_2, \dots, f_k). The subcarrier channels are then combined together, creating a single composite RF signal consisting of k independent subcarrier channels. Subsequently, the composite RF signal is used to modulate an ITU wavelength via a dual-drive Mach-Zehnder (MZI) electro-optical modulator [1].

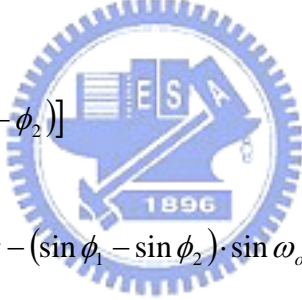
The composite modulating signal from an SCM block (see Fig. 2.1) was applied to both electrodes of the MZI modulator, with a $\pi/2$ relative phase shift between the arms. A DC bias sets the modulator at a quadrature point. Note that if a $\pi/2$ phase shift cannot be met over a wide frequency range, multiple phase shifters will have to be built. Thereafter, a number of wavelengths ($\lambda_1, \lambda_2, \dots, \lambda_N$), each carrying plural single-sided SCM signals, are combined by a conventional DWDM multiplexer onto the same fiber. At the receiving

terminal, these wavelengths are demultiplexed and a high-speed photo-detector converts the composite SCM signals in a single wavelength back to their original RF frequencies. The composite SCM signal is then separated into constituent signals by a sequence of electrical frequency converters, filters, demodulators, and decoders.

2.2 Nonlinear Distortions in an SSB/SCM Transmission System — Single Subcarrier Channel

2.2.1 Third Order Harmonic Due to MZI Modulator

The output electrical field of a differential dual-electrode MZI modulator can be written as

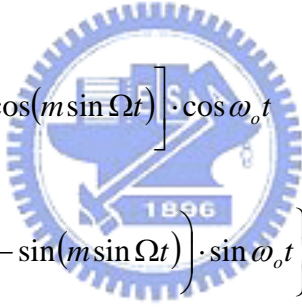


$$E_{out} = \frac{E_{in}}{\sqrt{2}} [\cos(\omega_o t + \phi_1) + \cos(\omega_o t - \phi_2)] \quad (2.1)$$

$$= \frac{E_{in}}{\sqrt{2}} [(\cos \phi_1 + \cos \phi_2) \cdot \cos \omega_o t - (\sin \phi_1 - \sin \phi_2) \cdot \sin \omega_o t] \quad (2.2)$$

where ω_o is the lightwave carrier angular frequency; E_{in} and E_{out} are the input and output electrical fields of the MZI modulator, respectively; ϕ_1 and ϕ_2 are the voltage-induced phase shifts of the two arms of the MZI modulator, both of which can be represented in the form of $\frac{\pi \cdot V_{dc}}{V_{\pi,dc}} + \frac{\pi \cdot V_{ac}(t)}{V_{\pi,ac}}$ (where $V_{\pi,dc}$ and $V_{\pi,ac}$ are the voltages required at DC bias port and RF input ports, respectively, to cause a 180-degree phase shift between the two interferometric arms). V_{dc} and $V_{ac}(t)$ are the DC bias voltage and RF drive signal, respectively. The opposite signs of ϕ_1 and ϕ_2 in the two cosine terms of (2.1) are attributed to the “differential” electrode configuration of the MZI modulator.

For SSB/SCM modulation, the RF signals at the two electrodes of a modulator must be a Hilbert transform pair, which means that one of the two RF signals has to pass through a 90° phase shifter. Furthermore, the modulator is DC biased at a quadrature point of the nonlinear E/O transfer curve of the modulator to avoid second-order nonlinear distortions. Therefore, if the modulator is modulated by $\cos(\Omega t)$, where Ω is a modulating RF frequency, ϕ_1 and ϕ_2 can be respectively represented as $\pi/2 + m \cdot \cos(\Omega t)$ and $m \cdot \sin(\Omega t)$, where $m = \pi \cdot V_{ac} / V_{\pi,ac}$ is the root-mean-square optical modulation index (RMS OMI). Note that $m^2/2$ is the normalized electrical power of the subcarrier channel at an RF input port of the MZI modulator. The output electrical field of the single RF-frequency modulated optical signal can then be obtained by rewriting (2.1) as



$$\begin{aligned}
 E_{out} &= \frac{E_{in}}{\sqrt{2}} \left\{ \left[\cos\left(\frac{\pi}{2} + m \cos \Omega t\right) + \cos(m \sin \Omega t) \right] \cdot \cos \omega_o t \right. \\
 &\quad \left. - \left(\sin\left(\frac{\pi}{2} + m \cos \Omega t\right) - \sin(m \sin \Omega t) \right) \cdot \sin \omega_o t \right\} \\
 &= \frac{E_{in}}{\sqrt{2}} \left\{ \sqrt{2} J_0(m) \cdot \cos\left(\omega_o t + \frac{\pi}{4}\right) - 2 J_1(m) \cdot \cos[(\omega_o + \Omega) \cdot t] \right. \\
 &\quad + \sqrt{2} J_2(m) \cdot \left\{ \cos\left[(\omega_o + 2\Omega) \cdot t - \frac{\pi}{4}\right] + \cos\left[(\omega_o - 2\Omega) \cdot t - \frac{\pi}{4}\right] \right\} \\
 &\quad + 2 J_3(m) \cdot \cos[(\omega_o - 3\Omega) \cdot t] \\
 &\quad + \sqrt{2} J_4(m) \cdot \left\{ \cos\left[(\omega_o + 4\Omega) \cdot t + \frac{\pi}{4}\right] + \cos\left[(\omega_o - 4\Omega) \cdot t + \frac{\pi}{4}\right] \right\} \\
 &\quad \left. - 2 J_5(m) \cdot \cos[(\omega_o + 5\Omega) \cdot t] + \dots \right\} \tag{2.3}
 \end{aligned}$$

where we have used Bessel function expansion to obtain (2.3), and $J_k(\cdot)$ ($k=1,2,3\dots$) is the Bessel function of the first kind, k th order. As expected, the electrical field is

composed of, in addition to the single-sided fundamental modulating frequency, an infinite number of harmonics of the modulating frequency. The even harmonics are double-sided, whereas the odd harmonics consist of alternative upper or lower sidebands at different orders. Fig. 2.2 shows the optical spectrum of a single channel SSB/SCM signal.

If only transmission loss is considered, the detected photocurrent is given by

$$I = \Re \cdot \eta \cdot |E_{out}|^2 \approx \frac{\Re \eta |E_{in}|^2}{2} \left\{ J_0^2(m) - 2\sqrt{2} J_0(m) J_1(m) \cdot \cos\left(\Omega t - \frac{\pi}{4}\right) + 2\sqrt{2} [J_0(m) J_3(m) - J_1(m) J_2(m)] \cdot \cos\left(3\Omega t + \frac{\pi}{4}\right) + \dots \right\} \quad (2.4)$$

where \Re is the photodiode responsivity, and η is the optical power attenuation. The first term $\Re \eta |E_{in}|^2 J_0^2(m)/2 = P_r \Re$ is the average photocurrent, and P_r is the received optical power. Note that the result contains no even order harmonics, as can be seen in (2.4). The third order harmonic distortion (HD3) due to the intrinsic nonlinear E/O “cosine” transfer curve of an MZI modulator, while using SSB/SCM modulation without considering fiber dispersions, is given by

$$HD3_{SSB/SCM,MZI} = \left[\frac{J_0(m) J_3(m) - J_1(m) J_2(m)}{J_0(m) J_1(m)} \right]^2 \quad (2.5)$$

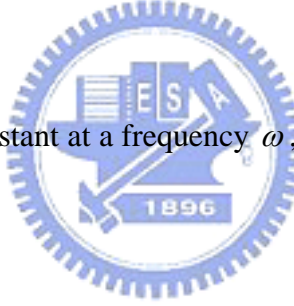
2.2.2 Second and Third Order Harmonic Distortions due to Linear Fiber Dispersion

Eq.(2.3) can be modified to include the effect of linear fiber dispersion in a transmission link. The electrical field of an SSB/SCM signal after propagating through a SMF with a

length z is given by

$$\begin{aligned}
E_{out,D} = & \frac{E_{in}}{\sqrt{2}} \left\{ \sqrt{2} J_0(m) \cdot \cos \left(\omega_o t + \frac{\pi}{4} - \beta_{\omega_o} z \right) - 2 J_1(m) \cdot \cos \left[(\omega_o + \Omega) \cdot t - \beta_{\omega_o + \Omega} z \right] \right. \\
& + \sqrt{2} J_2(m) \cdot \left\{ \cos \left[(\omega_o + 2\Omega) \cdot t - \frac{\pi}{4} - \beta_{\omega_o + 2\Omega} z \right] + \cos \left[(\omega_o - 2\Omega) \cdot t - \frac{\pi}{4} - \beta_{\omega_o - 2\Omega} z \right] \right\} \\
& + 2 J_3(m) \cdot \cos \left[(\omega_o - 3\Omega) \cdot t - \beta_{\omega_o - 3\Omega} z \right] \\
& + \sqrt{2} J_4(m) \cdot \left\{ \cos \left[(\omega_o + 4\Omega) \cdot t + \frac{\pi}{4} - \beta_{\omega_o + 4\Omega} z \right] + \cos \left[(\omega_o - 4\Omega) \cdot t + \frac{\pi}{4} - \beta_{\omega_o - 4\Omega} z \right] \right\} \\
& \left. - 2 J_5(m) \cdot \cos \left[(\omega_o + 5\Omega) \cdot t - \beta_{\omega_o + 5\Omega} z \right] + \dots \right\} \tag{2.6}
\end{aligned}$$

where β_ω is the propagation constant at a frequency ω , which can be expanded around an optical carrier frequency ω_o as



$$\beta_\omega = \beta_0 + \beta_1 (\omega - \omega_o) + \frac{1}{2} \beta_2 (\omega - \omega_o)^2 \tag{2.7}$$

where the higher order dispersion terms are neglected. β_1 and β_2 denote the first and second derivatives of the propagation constant with respect to the optical carrier frequency, respectively. The propagation phase shift, $\beta_\omega z$, for each optical subcarrier term is different due to the change in the refractive index as a function of the frequency. The SSB/SCM signal propagates in a fiber link with a group velocity $1/\beta_1$, and the fiber dispersion D is related to the group velocity dispersion parameter β_2 by $D = -2\pi c \beta_2 / \lambda^2$ where λ is the operating wavelength and c the velocity of light in

vacuum.

According to (2.6), the detected photocurrent can be written as

$$\begin{aligned}
 I = \Re \cdot \eta \cdot |E_{out,D}|^2 &\approx \frac{\Re \eta |E_{in}|^2}{2} \left\{ J_0^2(m) - 2\sqrt{2}J_0(m)J_1(m) \cdot \cos\left(\Omega t - \beta_1 \Omega z - \frac{1}{2}\beta_2 \Omega^2 z - \frac{\pi}{4}\right) \right. \\
 &\quad - 4J_0(m)J_2(m) \sin\left(\frac{1}{2}\beta_2(2\Omega)^2 z\right) \cdot \cos(2\Omega t - \beta_1(2\Omega)z) \\
 &\quad + 2\sqrt{2}C_1 \cdot \cos\left(3\Omega t - \beta_1(3\Omega)z + \frac{\pi}{4}\right) \\
 &\quad \left. - 2\sqrt{2}C_2 \cdot \sin\left(3\Omega t - \beta_1(3\Omega)z + \frac{\pi}{4}\right) + \dots \right\} \tag{2.8}
 \end{aligned}$$

where

$$\begin{aligned}
 C_1 &= J_0(m)J_3(m) \cos\left(\frac{1}{2}\beta_2(3\Omega)^2 z\right) - J_1(m)J_2(m) \cos\left(\frac{1}{2}\beta_2 3\Omega^2 z\right) \\
 C_2 &= J_0(m)J_3(m) \sin\left(\frac{1}{2}\beta_2(3\Omega)^2 z\right) - J_1(m)J_2(m) \sin\left(\frac{1}{2}\beta_2 3\Omega^2 z\right)
 \end{aligned}$$

Note that higher-order harmonics have been neglected in (2.8). Based on (2.8), we can see that when SSB/SCM modulation is used and a fiber transmission link with a distance z is considered, the normalized second and third order harmonic distortions are given by

$$HD2_{SSB/SCM,D} = 2 \left[\frac{J_2(m) \sin\left(\frac{1}{2}\beta_2(2\Omega)^2 z\right)}{J_1(m)} \right]^2 \tag{2.9}$$

$$HD3_{SSB/SCM,D} = \frac{C_1^2 + C_2^2}{J_0^2(m)J_1^2(m)} \tag{2.10}$$

2.3 Nonlinear Distortions in an SSB/SCM Transmission System — Multiple Subcarrier Channels

2.3.1 CTB Distortions Due to MZI Modulator

The derivations in Sec. 2.2 can be extended to the case of multiple subcarrier channels, i.e., ϕ_1 and ϕ_2 in (2.1) can be replaced by $\pi/2 + m \cdot \sum_i \cos(\Omega_i t)$ and $m \cdot \sum_i \sin(\Omega_i t)$, respectively, Ω_i is the radian carrier frequency of the subcarrier channel i , and all channels have the same RMS OMI value, m . Fig. 2.3 shows the optical spectrum of a 2-ch SSB/SCM signal. The resultant SSB/SCM-modulation 3rd order nonlinear distortions (NLDs) are summarized in Table 2.1.

It is well known that when the number of subcarrier channels is large, the dominant 3rd order NLD is the triple beat product, which is expressed in decibels as

$$CTB_{SSB/SCM,MZI} = 10 \cdot \log \left\{ 4 \cdot \left[\frac{J_1(m)}{J_0(m)} \right]^4 \cdot N_{CTB} \right\} \quad (2.11)$$

where N_{CTB} is the triple-beat product count at a particular subcarrier channel of interest, whose center frequency Ω_d is equal to $\Omega_i \pm \Omega_j \pm \Omega_k$.

2.3.2 CSO due to Linear Fiber Dispersion

The derivations in Sec. 2.2.2 can be extended to the case of multiple subcarrier channels, and we summarize the results of various 2nd order NLDs in a transmission system using conventional single-mode fiber with a length of z in Table 2.2.

The second order intermodulation distortion terms include two categories, IM_{i+j} and IM_{i-j} , as a result of SSB/SCM modulation. The reason why the amplitudes of IM_{i+j} and IM_{i-j} are different can be explained as follows. IM_{i+j} results from two types of beatings, i.e., ω_o beats with $[\omega_o + (\Omega_1 + \Omega_2)]$ or $[\omega_o - (\Omega_1 + \Omega_2)]$; while IM_{i-j} results from three types of beatings, i.e., in addition to ω_o beating with $[\omega_o + (\Omega_1 - \Omega_2)]$ or $[\omega_o - (\Omega_1 - \Omega_2)]$, there is a third contributing term from the beating between $(\omega_o - \Omega_1)$ and $(\omega_o - \Omega_2)$.

Note that IM_{i-j} in Table 2.2 is not only distortion frequency (Ω_d) dependent, but also is source frequency (Ω_i and Ω_j) dependent.



When the number of subcarrier channels is large, the dominant 2nd order NLD is the combination of IM_{i+j} and IM_{i-j} , and is expressed in decibels as

$$CSO_{SSB/SCM,D} = 10 \cdot \log \left\{ IM_{i+j} \cdot N_{\Omega_i + \Omega_j = \Omega_d} + \sum_{\Omega_i - \Omega_j = \Omega_d} IM_{i-j} \right\} \quad (2.12)$$

where Ω_i and Ω_j should be arbitrarily chosen from the frequencies of multiple subcarrier channels and $N_{\Omega_i + \Omega_j = \Omega_d}$ is the number of second order intermodulation components whose source beating-frequencies satisfy $\Omega_i + \Omega_j = \Omega_d$. On the other hand,

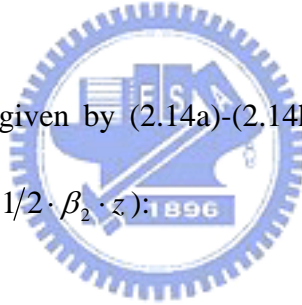
when the distortion is source beating-frequency dependent, the accumulation of the second order intermodulation distortions should be rewritten as the summation form such as the second term in (2.12).

2.3.3 CTB due to Linear Fiber Dispersion

The derivations on linear fiber dispersion-induced harmonic distortions in Sec. 2.2 can be extended to third-order intermodulation distortions as follows:

$$IM_{i\pm j\pm k} = \left[\frac{J_1(m)}{J_0(m)} \right]^4 \cdot (C1_{i\pm j\pm k}^2 + C2_{i\pm j\pm k}^2) \quad (2.13)$$

where $C1_{i\pm j\pm k}$ and $C2_{i\pm j\pm k}$ are given by (2.14a)-(2.14h) shown below (note that ρ in these equations is again given by $1/2 \cdot \beta_2 \cdot z$).



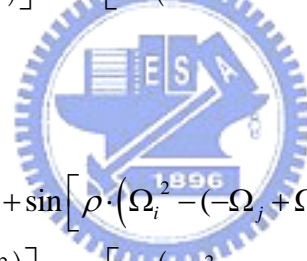
$$C1_{i+j+k} = \cos[\rho \cdot (\Omega_i + \Omega_j + \Omega_k)^2] - \cos[\rho \cdot (\Omega_i^2 - (\Omega_j + \Omega_k)^2)] - \cos[\rho \cdot (\Omega_j^2 - (\Omega_i + \Omega_k)^2)] - \cos[\rho \cdot (\Omega_k^2 - (\Omega_i + \Omega_j)^2)] \quad (2.14a)$$

$$C2_{i+j+k} = \sin[\rho \cdot (\Omega_i + \Omega_j + \Omega_k)^2] + \sin[\rho \cdot (\Omega_i^2 - (\Omega_j + \Omega_k)^2)] + \sin[\rho \cdot (\Omega_j^2 - (\Omega_i + \Omega_k)^2)] + \sin[\rho \cdot (\Omega_k^2 - (\Omega_i + \Omega_j)^2)] \quad (2.14b)$$

$$C1_{i+j-k} = -\cos[\rho \cdot (\Omega_i + \Omega_j - \Omega_k)^2] - \cos[\rho \cdot (\Omega_i^2 - (\Omega_j - \Omega_k)^2)] \\ - \cos[\rho \cdot (\Omega_j^2 - (\Omega_i - \Omega_k)^2)] + \cos[\rho \cdot (\Omega_k^2 - (\Omega_i + \Omega_j)^2)] \quad (2.14c)$$

$$C2_{i+j-k} = \sin[\rho \cdot (\Omega_i + \Omega_j - \Omega_k)^2] + \sin[\rho \cdot (\Omega_i^2 - (\Omega_j - \Omega_k)^2)] \\ + \sin[\rho \cdot (\Omega_j^2 - (\Omega_i - \Omega_k)^2)] + \sin[\rho \cdot (\Omega_k^2 - (\Omega_i + \Omega_j)^2)] \quad (2.14d)$$

$$C1_{i-j+k} = -\cos[\rho \cdot (\Omega_i - \Omega_j + \Omega_k)^2] - \cos[\rho \cdot (\Omega_i^2 - (-\Omega_j + \Omega_k)^2)] \\ + \cos[\rho \cdot (\Omega_j^2 - (\Omega_i + \Omega_k)^2)] - \cos[\rho \cdot (\Omega_k^2 - (\Omega_i - \Omega_j)^2)] \quad (2.14e)$$



$$C2_{i-j+k} = \sin[\rho \cdot (\Omega_i - \Omega_j + \Omega_k)^2] + \sin[\rho \cdot (\Omega_i^2 - (-\Omega_j + \Omega_k)^2)] \\ + \sin[\rho \cdot (\Omega_j^2 - (\Omega_i + \Omega_k)^2)] + \sin[\rho \cdot (\Omega_k^2 - (\Omega_i - \Omega_j)^2)] \quad (2.14f)$$

$$C1_{i-j-k} = \cos[\rho \cdot (\Omega_i - \Omega_j - \Omega_k)^2] - \cos[\rho \cdot (\Omega_i^2 - (-\Omega_j - \Omega_k)^2)] \\ + \cos[\rho \cdot (\Omega_j^2 - (\Omega_i - \Omega_k)^2)] + \cos[\rho \cdot (\Omega_k^2 - (\Omega_i - \Omega_j)^2)] \quad (2.14g)$$

$$C2_{i-j-k} = \sin[\rho \cdot (\Omega_i - \Omega_j - \Omega_k)^2] + \sin[\rho \cdot (\Omega_i^2 - (-\Omega_j - \Omega_k)^2)] \\ + \sin[\rho \cdot (\Omega_j^2 - (\Omega_i - \Omega_k)^2)] + \sin[\rho \cdot (\Omega_k^2 - (\Omega_i - \Omega_j)^2)] \quad (2.14h)$$

We can write the composite triple beat (CTB) in decibel as:

$$CTB_{SSB/SCM,D} = 10 \cdot \log \left(\sum_{\Omega_i \pm \Omega_j \pm \Omega_k = \Omega_d} IM_{i \pm j \pm k} \right) \quad (2.15)$$

where Ω_i , Ω_j and Ω_k could be chosen arbitrarily from the frequencies of multiple subcarrier channels and Ω_d is the distortion frequency.

2.3.4 Theoretical Predictions and Simulation Results

Computer simulations were carried out to verify the analytical results derived in Sec. 2.3.1 to 2.3.3, and the results are given below. Note that we used a time window (the reciprocal of "frequency resolution") of $128/155e6$ sec, and a sample rate of $8 \times 64 \times 155e6$ Hz (79.36GHz).

To verify the results derived in Sec. 2.3.1 and 2.3.2, we used 64 channels of QPSK signals in the frequency range from 0.93 to 12.648 GHz. RMS OMI per channel was assumed to be 4%. Each QPSK signal has a symbol rate of 155 Msps and an excess bandwidth factor of 0.2; and the channel spacing is 186 MHz (1.2×155 MHz). Bit-streams among those 64 channels were assumed to be uncorrelated.

To study the fundamental nonlinear distortions due to intrinsic MZ modulator nonlinearity and fiber dispersion, thermal and shot noise are not taken into account. At the receiver end, noise-to-signal ratio (NSR) is measured to estimate the impact of NLDs. CW

RF/microwave tones are used to represent the modulated signals [5].

Two cases were studied: *back-to-back* and *80 km SMF transmission* (with a fiber dispersion of 17 ps/nm/km at 1.55 μm). In both cases, after all subcarrier channels were converted to electrical signals by a photodiode, one of the 64 channels was sampled and electrically filtered to measure its NSR performance. The sampled channel should be turned off while measuring the total noise-like NLD in its bandwidth. Since different orders of NLD falling into a particular channel cannot be separated in the simulation, we need to know the dominant NLD in each case — for the case of back-to-back, the dominant NLD is CTB due to MZI modulator, and it is the fundamental system limit even when all fiber dispersions are compensated; for the case of 80 km transmission, the dominant NLD is CSO.

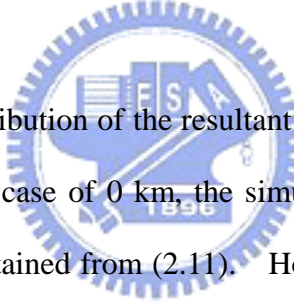


Fig. 2.4 shows the frequency distribution of the resultant NSR for transmission lengths of 0 and 80 km, respectively. In the case of 0 km, the simulation result agrees well with the analytical CTB approximation obtained from (2.11). However, in the case of 80 km SMF fiber transmission, although the simulation result agrees quite well with the analytical CSO approximation obtained from (2.12) in most cases, there does exist some large discrepancy at those frequencies close to dips. This is because at those dips, CTBs due to linear fiber dispersion are not negligible.

Note that in general CSO is proportional to m^2 while CTB is proportional to m^4 , as can be observed from Eqs. (2.11) and (2.12) by letting $J_0(m) \approx 1$, $J_1(m) \approx m$, $J_2(m) \approx m^2/2$ and $J_3(m) \propto m^3$ for $\text{RMS OMI}/ch \ll 1$. Therefore, in a multi-channel, dispersive system with small $\text{RMS OMI}/ch$, CSOs are the dominant nonlinear terms.

Fig. 2.5 shows the linear fiber dispersion-induced CSO as a function of transmission distance. At an OMI/ch of 4%, the CSO in channel 32 (dashed line) first monotonously increases with transmission distance until at about 50 km and then fluctuates around ~ -14 dB with a peak-to-peak variation of ~ 2.5 dB. This phenomenon may be explained from IM_{i-j} in (2.12), where each contribution has distance-dependent cosine or sine terms and with different period along the transmission distance z . The solid line in Fig. 2.5 represents the CSO in a worst-case channel at different distances. Note that the worst-case channel is not a fixed channel, rather, it is distance-dependent, i.e., for each distance, the worst CSO may occur in different channels. It can be seen that the worst-case CSO increases with distance initially, but saturates at ~ -10 dB beyond about 100 km.

It is of interest to compare SSB/SCM system to a conventional SCM system, in which two sidebands exist on each side of an optical carrier. The transmission distance of the latter is known to be bounded by the dispersion-limited bandwidth [6], rather than by CSOs. The limited transmission bandwidth is caused by the periodic cancellation of the two sidebands. For example, when a conventional SCM system has the same maximum microwave subcarrier frequency of 12.648 GHz as the current SSB/SCM system, its transmission distance is limited to only ~ 23 km.

To verify the results derived in Sec. 2.3.3, a computer simulation on fiber dispersion-induced CTB was carried out for the case of 32 16-QAM signals between 6.882 and 12.648 GHz (within an octave), with an RMS OMI per channel of 1.8%. Fig. 2.6 shows the frequency distribution of the calculated and simulated NSR for transmission lengths of 0, 30 and 80 km, respectively. In the case of 0 km, the dominant NLD is the intrinsic MZI-induced CTB (see (2.11)). However, with fiber transmissions, the dominant

NLD becomes the fiber dispersion-induced CTB. It is clear that the simulation results agree well with the analytical CTB given in (2.15). Note the dispersion-induced CTB at 30 km is more severe than that at 80 km. This is because the dispersion-induced CTBs oscillate around the MZI-induced CTB, as shown in Fig. 2.7, and is due to the cosine and sine terms in (2.14a)-(2.14h).

Fig. 2.7 shows the linear fiber dispersion-induced CTB as a function of transmission distance. The intrinsic MZI-induced CTB of channel 16 (dotted line) obtained from (2.11) is shown as a distance-independent baseline. It is shown that the CTB in channel 16 (dashed line) irregularly oscillates around the baseline, and the deviation from the baseline becomes smaller as the distance increases. This may be attributed to the distance-dependent cosine and sine terms in (2.14a)-(2.14h). Note that the worst-case CTB which occurs in channel 16 has a maximum value of ~ -45 dB after a fiber transmission of ~ 30 km. Furthermore, the worst-case CTB approaches the baseline beyond a certain distance, i.e., 150 km in the current QAM/SSB/SCM system. This result has an important implication to future metro and wireless optical networks in that the transmission distance of a high-capacity SSB/SCM system can be essentially distance-independent, provided that all SCM channels can be kept within one octave.

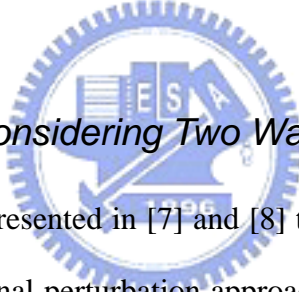
2.4 SPM-Induced Impairment

The effects of SPM in an SSB/SCM system include (1) SPM-induced subcarrier amplitude fluctuation which varies among multiple modulation frequencies (considering a fixed distance); (2) SPM and chromatic dispersion induced residual optical single sideband [14]; and (3) SPM-induced nonlinear distortions. We have found that the third factor is negligible when compared with the nonlinear distortions caused by linear fiber dispersion

and nonlinear cross-phase modulation (in the case of multiple wavelengths). The first and second factors can also be ignored if we limit the launched power per wavelength to below ~ 6 dBm, which gives a subcarrier to subcarrier amplitude variation of less than 1 dB [14], [19].

2.5 DWDM Configuration – XPM Limitations

In this section, the effect of XPM on SSB/SCM/DWDM optical fiber links is investigated theoretically and numerically. A generalized theoretical model of crosstalk (XT) induced by an arbitrary number of wavelength channels through XPM is derived, and is verified by computer simulations.



2.5.1 XPM-induced XT Considering Two Wavelengths

Here we generalize the analysis presented in [7] and [8] to obtain the results for SSB/SCM systems. Note that the small-signal perturbation approach shown in [4] cannot be applied to subcarrier frequencies higher than about 1 GHz, and is not applicable to the microwave SSB/SCM system under consideration. We first consider a CW probe wavelength and a modulated pump wavelength with the same polarization co-propagating in a single-mode optical fiber. At the fiber input, the expression for a sine-modulated pump channel is given by

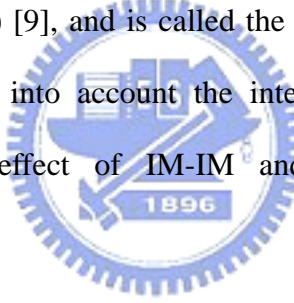
$$\tilde{P}_p(t) = m \bar{P}_p(0) \cdot \cos(\Omega t + \theta), \text{ (input pump)}$$

whose complex amplitude is given by $\tilde{P}_p(\Omega) = m \bar{P}_p(0) \cdot e^{j\theta}$, where $\bar{P}_p(0)$ is the average pump power at the fiber input. The change of the pump signal power due to both GVD

and fiber nonlinearity can modulate the phase of a probe channel through XPM. Let us assume the normalized complex amplitude of the pump signal at a distance z can be expressed as [8]

$$\tilde{P}_p(z, \Omega) = \tilde{P}_p(\Omega) \cdot H_{Fp}(z, \Omega) \cdot e^{-\alpha z} e^{-j\Omega z/v_{gp}}, \text{ (pump at a distance } z\text{)}$$

where $e^{-\alpha z} e^{-j\Omega z/v_{gp}}$ accounts for the attenuation and propagation delay at a distance z from the fiber input. Note that v_{gp} and α are the group velocity and attenuation coefficient, respectively. The function $H_{F_x}(z, \Omega)$ ($x = p$ for a pump channel, and $x = b$ for a probe channel) is defined as the ratio between the intensity modulation at the fiber output (at a distance z) and fiber input ($z = 0$) [9], and is called the intensity modulation-fiber transfer function (IM-FTF), which takes into account the interaction of fiber nonlinearity and dispersion. To separate the effect of IM-IM and PM-IM conversions, we can express $H_{F_x}(z, \Omega)$ as [9]–[15],



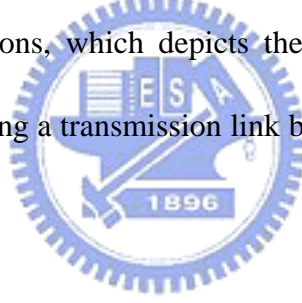
$$H_{F_x}(z, \Omega) = C_{IM-IM}(z, \Omega) + H_{PM}(\Omega) \cdot C_{PM-IM}(z, \Omega)$$

where $C_{IM-IM}(z, \Omega) = \tilde{p}_N(z, \Omega)/\tilde{p}_N(0, \Omega)|_{\tilde{\phi}(0, \Omega)=0}$ is a conversion function representing IM-IM conversion, $C_{PM-IM}(z, \Omega) = \tilde{p}_N(z, \Omega)/[2\bar{P}(0) \cdot \tilde{\phi}(0, \Omega)]|_{\tilde{p}_N(0, \Omega)=0}$ is a conversion function representing PM-IM conversion, and $H_{PM}(\Omega) = 2\bar{P}(0) \cdot \tilde{\phi}(0, \Omega)/\tilde{p}_N(0, \Omega)$ gives the relation between IM and PM for a given optical transmitter. Note that $\tilde{p}_N(z, \Omega)$ and $\tilde{\phi}(z, \Omega)$ are the Fourier transforms of the normalized signal power and phase terms $\tilde{p}_N(z, t)$ and $\tilde{\phi}(z, t)$ (normalized by $\bar{P}(0)$) of the pump channel (or probe channel),

respectively.

In a directly modulated semiconductor laser [10]–[12], $H_{PM}(\Omega) = \alpha_c(1 - j f_c/f)$, where α_c is the chirp parameter and f_c is the frequency at which the adiabatic chirp equals to the transient chirp. In an externally modulated IM-DD system [15], $H_{PM}(\Omega) = \alpha_c$. In an SSB/SCM modulation system with ideal dual-electrode MZI modulator [14], i.e., the case we are interested in, $H_{PM}(\Omega) = \pm j$ (+ j represents optical lower side band (LSB), whereas $-j$ represents optical upper side band (USB)).

For a given $H_{PM}(\Omega)$, one can numerically solve $C_{IM-IM}(z, \Omega)$, $C_{PM-IM}(z, \Omega)$ and $H_{F_x}(z, \Omega)$ (by using the fourth-fifth-order Runge-Kutta method) from the following coupled linear differential equations, which depicts the evolution of small-signal power $\tilde{p}_N(z, \Omega)$ and phase $\tilde{\phi}(z, \Omega)$ along a transmission link by considering both GVD and fiber nonlinearities [16]:



$$\frac{\partial \tilde{p}_N(z, \Omega)}{\partial z} = \beta_2 \Omega^2 \bar{P}(0) \cdot \tilde{\phi}(z, \Omega) \quad (2.16)$$

$$\frac{\partial \tilde{\phi}(z, \Omega)}{\partial z} = - \left[\frac{\beta_2 \Omega^2}{4 \bar{P}(0)} + \gamma \cdot \exp(-\alpha z) \right] \cdot \tilde{p}_N(z, \Omega) \quad (2.17)$$

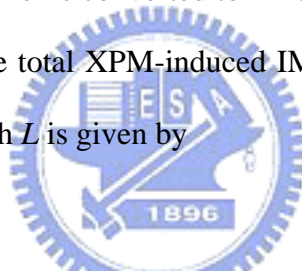
where β_2 is the first-order group velocity dispersion parameter presented in section 2.2, $\gamma = 2\pi n_2 / (\lambda A_{eff})$ is the nonlinearity coefficient accounting for the nonlinear Kerr effect, n_2 is the nonlinear refractive index, and A_{eff} the effective core area of the optical fiber.

Once $H_{Fp}(z, \Omega)$ is obtained, the XPM-induced complex sinusoidal PM in the probe channel (originated in an infinitesimal section of length dz at a distance z from the fiber input) is given by [8]

$$d\tilde{\phi}_{XPM}(z, \Omega) = -2\gamma_b \tilde{P}_p(\Omega) \cdot H_{Fp}(z, \Omega) \cdot e^{-\alpha z} e^{-j\Omega z/v_{gp}} dz \quad (\text{XPM-induced PM in a probe channel}), \quad (2.18)$$

where γ_b is the nonlinear coupling coefficient of a probe channel.

XPM-induced PM in a probe channel is converted to IM at the output of a transmission link through PM-IM conversion. The total XPM-induced IM of a probe channel at the output of a transmission link with a length L is given by



$$\tilde{P}_{XPM}(z, \Omega) = \int_0^L 2\bar{P}_b(z) \cdot e^{-\alpha(L-z)} e^{-j\Omega(L-z)/v_{gb}} \cdot C_{PM-IM,b}(L-z, \Omega) \cdot d\tilde{\phi}_{XPM}(z, \Omega) \quad (\text{PM-to-IM induced IM in a probe channel}), \quad (2.19)$$

where $\bar{P}_b(z) = \bar{P}_b(0) \cdot e^{-\alpha z}$ is the average power of the probe channel at a distance z , and $\bar{P}_b(0)$ is the average power of a probe channel at the fiber input; $e^{-\alpha(L-z)} e^{-j\Omega(L-z)/v_{gb}}$ represents the attenuation and propagation delay of the probe channel from z to L ; and $C_{PM-IM,b}(L-z, \Omega)$ is the PM-IM conversion of the probe channel from z to L .

Substituting Eqs. (2.18) into (2.19) yields

$$\tilde{P}_{XPM}(\Omega) = -4\gamma_b \bar{P}_b(0) \cdot \tilde{P}_p(\Omega) \cdot e^{-\alpha L} e^{-j\Omega L/v_{gb}} \cdot \int_0^L \exp(-\sigma z) \cdot H_{Fp}(z, \Omega) \cdot C_{PM-IM,b}(L-z, \Omega) \cdot dz \quad (2.20)$$

where $\sigma = \alpha - j\Omega d_{bp}$ and $d_{bp} \equiv (v_{gb})^{-1} - (v_{gp})^{-1} = \int_{\lambda_p}^{\lambda_b} D(\lambda) d\lambda$ is the walk-off parameter between pump and probe wavelengths. In a non-zero dispersion region, $d_{bp} \approx D_b \cdot \Delta\lambda_{bp} - S_b \cdot (\Delta\lambda_{bp})^2$, where $\Delta\lambda_{bp} \equiv \lambda_b - \lambda_p$ is the separation between probe and pump wavelengths, and $S_b \equiv dD/d\lambda|_{\lambda_b}$ is the dispersion slope of the probe channel.

Note that $H_{Fp}(z, \Omega)$ in (2.20), instead of being numerically obtained via (2.16) and (2.17), can possibly be approximated by using a closed-form obtained from a linear dispersive system. In the next Section, we will point out the limitation of this approach, despite that it could save significant computing time and help us gain more physical insights. The IM-IM and PM-IM conversions of a pump channel can be expressed by [9]

$$C_{IM-IM,p}(z, \Omega) = \cos(\Theta_p z) \quad \text{and} \quad C_{PM-IM,p}(z, \Omega) = -\sin(\Theta_p z) , \quad \text{respectively, where}$$

$$\Theta_p = \Omega^2 D_p \lambda_p^2 / (4\pi c) \quad \text{with } D_p \text{ being the dispersion coefficient of the pump channel.}$$

Consequently, the IM-FTF of a pump channel is given by a simplified expression:

$$H_{Fp}(z, \Omega) = \cos(\Theta_p z) - H_{PM}(\Omega) \cdot \sin(\Theta_p z).$$

In an USB/SCM system, $H_{Fp}(z, \Omega) = H_{Fp,USB}(z, \Omega) = \cos(\Theta_p z) + j \cdot \sin(\Theta_p z)$ and $C_{PM-IM,b}(L-z, \Omega) = -\sin[\Theta_b(L-z)]$ can be used in (2.20) to obtain a closed-form solution as

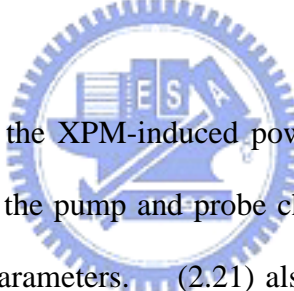
$$\tilde{P}_{XPM,USB}(\Omega) = 4\gamma_b \bar{P}_b(0) \cdot \tilde{P}_p(\Omega) \cdot e^{-\alpha L} e^{-j\Omega L/v_{gb}}$$

$$\cdot \left\{ \frac{1}{(\sigma - j\Theta_p)^2 + \Theta_b^2} \left[(\sigma - j\Theta_p) \cdot \sin(\Theta_b L) - \Theta_b \cdot \cos(\Theta_b L) + \Theta_b \cdot e^{-(\sigma - j\Theta_p)L} \right] \right\} \quad (2.21)$$

For an LSB/SCM system, the result in (2.21) can be modified by replacing $j\Theta_p$ with

$-j\Theta_p$. The XT induced by XPM in a probe channel is given by

$XT_{XPM} = \left| \tilde{P}_{XPM}(\Omega) / \left(\tilde{P}_p(\Omega) \cdot e^{-\alpha L} \right) \right|^2$, where $\tilde{P}_p(\Omega)$ is the complex amplitude of a pump channel.



(2.21) shows that the strength of the XPM-induced power fluctuation in a probe channel depends on the average power of the pump and probe channels, the modulation frequency Ω , the walk-off and dispersion parameters. (2.21) also shows that in general the major contribution to the XPM-induced XT is generated in the front part of the fiber as a result of the optical power attenuation $e^{-\alpha L}$. (2.21) further shows that only when there is a local zero fiber dispersion at the probe wavelength (i.e., $\Theta_b = 0$) can the XPM-induced XT be eliminated.

If we rewrite the term $\sigma - j\Theta_p$ in (2.21) as $\alpha - j(\Omega d_{bp} \pm \Theta_p)$, we can see that when Θ_p and the walk-off parameter Ωd_{bp} have the same sign, Θ_p increases the walk-off; whereas when they have different signs, Θ_p decreases the walk-off. It is interesting to see that the phase change effect due to GVD in SSB/SCM modulation is significantly comparable to

the walk-off effect at a small channel separation and at a high modulation frequency. This

can be easily observed from the ratio of Θ_p and Ωd_{bp} , given by $\frac{\Omega/\omega_p}{2\Delta\lambda_{bp}/\lambda_p}$, where ω_p

is the optical angular frequency of the pump channel. For example, when the wavelength separation is 0.2 nm and the modulation frequency is 1 GHz, the ratio of Θ_p and Ωd_{bp} is about 1/50, and therefore Θ_p is negligible. Following the same logic, this is also true when the channel spacing is more than 0.2 nm. However, when the modulation frequency is increased to $>\sim 10$ GHz, Θ_p becomes comparable to Ωd_{bp} and cannot be neglected.

From the above discussion, it is possible to further simplify (2.21) by letting $\Theta_p=0$ when

the WDM channel spacing is larger than 0.2 nm and when the RF modulation frequency is lower than a few GHz. Under this condition, we have $H_{Fp}(z, \Omega) \approx 1$, $\cos(\Theta_b L) \approx 1$, and $\sin(\Theta_b L) \approx \Omega^2 D_b \lambda_b^2 L / (4\pi c)$. Consequently, XT based on (2.21) can be approximated as

[4], [8]

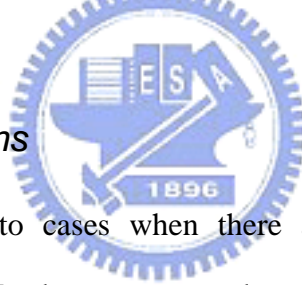
$$XT_{XPM}(\Omega) = \left| \gamma_b \bar{P}_p(0) \cdot \frac{\lambda_b^2}{\pi c} D_b L \frac{\Omega^2}{\alpha - j\Omega d_{bp}} \cdot \left[1 - \frac{1 - e^{-(\alpha - j\Omega d_{bp})L}}{\alpha - j\Omega d_{bp}} \right]^2 \right| \quad (2.22)$$

It can be seen from (2.22) that for a weak walk-off and small modulation frequencies,

$|\Omega d_{dp}| \ll \alpha$, the XPM-induced XT increases linearly with Ω^4 ; while for a strong walk-off and higher modulation frequencies, $|\Omega d_{dp}| \gg \alpha$, the XPM-induced XT is linearly proportional to Ω^2 , and inversely proportional to the square of channel spacing. Also

note that XPM-induced XT is independent of *OMI/ch*.

Under the conditions of large wavelength spacing and small modulation frequencies, both an SSB/SCM system and a dispersion-compensated optical double sideband (ODSB) system have neither dispersion-induced fading nor pump envelope change, i.e., $|H_{Fp}(z, \Omega)| = 1$ (note that an ODSB system without dispersion compensation has $H_{Fp}(z, \Omega) = \cos(\Theta_p z)$). It should be noted, however, that in an SSB/SCM system $H_{Fp}(z, \Omega) = \cos(\Theta_p z) \pm j \cdot \sin(\Theta_p z) = \exp(\pm j\Theta_p z)$ (+: USB; -: LSB), hence $|H_{Fp}(z, \Omega)| = 1$ does not imply $\Theta_p = 0$. Consequently, the assumption of $\Theta_p = 0$ may cause errors, which we will discuss subsequently.



2.5.2 Multiple Wavelengths

(2.18) can be easily extended to cases when there are more than two wavelengths co-propagating in a fiber link. In those cases, each pump wavelength k modulates the phase of a probe wavelength independently [17], [18] and therefore (2.18) can be modified as

$$d\tilde{\phi}_{XPM, total}(z, \Omega) = -2\gamma_b \left[\sum_{k \neq b} \tilde{P}_k(\Omega) \cdot H_{Fk}(z, \Omega) \cdot e^{-j\Omega z / v_{gk}} \right] \cdot e^{-\alpha z} dz \quad (2.23)$$

where $\tilde{P}_k(\Omega)$ and $H_{Fk}(z, \Omega)$ are the complex amplitude and the IM-FTF of pump channel k , respectively. The total power fluctuation induced by XPM in a probe channel at the output of a fiber link can be written as $\tilde{P}_{XPM, total}(\Omega) = \sum_{k \neq b} \tilde{P}_{XPM, bk}(\Omega)$ with each individual

$\tilde{P}_{XPM,bk}(\Omega)$ given by (2.20) or (2.21). When random phase relationship of the modulating signals in each wavelength is assumed, the total XPM-induced XT in a probe channel can be expressed by

$$XT_{XPM,total} = \sum_{k \neq b} \left| \tilde{P}_{XPM,bk}(\Omega) / \left(\tilde{P}_b(\Omega) \cdot e^{-\alpha L} \right) \right|^2 \quad (2.24)$$

2.5.3 Transmission Link Performance due to XPM: Simulation, Numerical, and Theoretical Results

To validate the theoretical results on XPM-induced XT, we carried out numerical calculations and computer simulations on a system with parameters shown in Table 2.3. The system is a 64-channel 155 Msps QPSK USB/SCM transmission system over 80 km of conventional SMF, and has a theoretical transport capacity of 20 Gbps per wavelength.



1) Two Wavelengths: Assuming a pump wavelength is modulated by 64-channel QPSK signals occupying a frequency range beyond an octave, the distribution of XT at different RF frequencies in a co-propagating probe wavelength is shown in Fig. 2.8. Three average optical power levels per wavelength were studied: 0, 6 and 10 dBm.

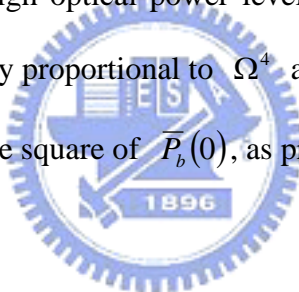
Simulation results are shown by circles ($\Delta\lambda_{bp} = -0.2$ nm, i.e., $\lambda_b - \lambda_p = -0.2$ nm) or triangles ($\Delta\lambda_{bp} = +0.2$ nm, but only for input power of 0 dBm per wavelength). Note that in the simulation, the digital modulation data among different RF channels were carefully kept independent. Also, we used a time window of 128/155e6 sec, and a sample rate of $8 \times 8 \times 64 \times 155e6$ Hz (634.88 GHz).

Numerical results obtained from (2.20) and the coupled nonlinear Schrödinger equations (2.16) and (2.17) are shown by solid lines.

Theoretical results obtained from (2.21) ($\Theta_p \neq 0$, dotted line; and $\Theta_p = 0$, dashed line) are also shown in Fig. 2.8.

Several observations from Fig. 2.8 are summarized below:

- The numerical results show an excellent agreement with those of simulations, even in the case of a high optical power level of 10 dBm per wavelength. In general, The XT is nearly proportional to Ω^4 at low modulation frequencies, and nearly proportional to the square of $\bar{P}_b(0)$, as predicted by (2.22).



Theoretical results based on (2.21) ($\Theta_p \neq 0$) agree very well with simulation results (within ~ 2 dB). The ~ 2 dB discrepancy occurs only at the case of 10 dBm/ λ with a modulation frequency $> \sim 8$ GHz. This discrepancy may be attributed to two factors. The first is that at a very high input power per wavelength, the linear-system-approximated IM-FTF $H_{Fp}(z, \Omega) = \cos(\Theta_p z) \pm j \cdot \sin(\Theta_p z)$ is no longer valid. This is because the interaction between SPM and chromatic dispersion could generate a second residual optical single-sideband [14], causing two optical sidebands to interfere with each other at the receiver. The second is that a high input power could cause enhanced IM-IM and PM-IM conversions, and in addition, the

fading-induced dip frequency could shift toward slightly higher frequencies [13], [14], [19].

- The theoretical approximation based on (2.21) ($\Theta_p = 0$) is seen to cause more errors in the higher modulation frequency range when compared to the more exact theoretical estimation based on $\Theta_p \neq 0$.
- At a launched power of 0 dBm per wavelength, the XT of $\Delta\lambda_{bp} = -0.2$ nm is always greater than that of $\Delta\lambda_{bp} = +0.2$ nm by up to ~ 5 dB. The difference is more pronounced at higher modulation frequencies. This confirms what we said earlier about the pump phase change along the fiber (caused by the combined effects of SSB/SCM modulation and GVD) could enhance or mitigate the walk-off effect. Since we used USB/SCM here, the walk-off effect will be affected via $\alpha - j(\Omega d_{bp} + \Theta_p)$ (see (2.21)). Considering 1550 nm wavelength propagating in a conventional SMF, the dispersion is positive, and therefore Θ_p is positive. Consequently, a negative $\Delta\lambda_{bp}$ ($\Omega d_{bp} < 0$) will generate more XPM-induced XT than a positive $\Delta\lambda_{bp}$ ($\Omega d_{bp} > 0$), because the latter enhances the walk-off effect.
- The CNR requirement of a QPSK signal is 17 and 20 dB in theory and practice, respectively. Therefore, the power level per wavelength should be kept below ~ 3 dBm in this transmission system.
- A dip frequency occurs at somewhere between 9.6 to 9.8 GHz under different conditions. This is due to the fact that PM-IM conversion vanishes around 9.6 GHz for a SMF fiber length of 80 km, i.e., $\Theta_b z = n\pi$ in

$C_{PM-IM,b}(z, \Omega) = -\sin(\Theta_b z)$, and therefore the XT performance is improved.

2) Four Wavelengths: Fig. 2.9 shows the XPM-induced XT due to four adjacent wavelengths (spaced at 25, 50, or 100 GHz) for the system given in Table 2.3. The average optical power per wavelength is 6 dBm. The probe channel is located at the center (λ_3 in the inset of Fig. 2.9). Simulation results are shown in circles, numerical results (using (2.16), (2.17) (2.20) and (2.24)) are shown in solid lines, and theoretical results (using (2.21) and (2.24)) are shown in dotted lines. The followings can be observed in Fig. 2.9:

- All results from simulations, numerical calculations, and theory match very well. However, it should be noted that at higher power levels (e.g., 10 dBm), the influence of fiber nonlinearity on the PM-IM conversion becomes non-negligible and the small-signal analysis results used to derive (2.21) may no longer be valid.
- The XT is nearly inversely proportional to the square of wavelength separation for moderate to high frequencies, as predicted by (2.22).
- It can be predicted that the XT estimates based on either $\Theta_p \neq 0$ or $\Theta_p = 0$ (not shown in figure) will have a negligible difference (within 1 dB for 0.2 nm wavelength separation). This is because, from the viewpoint of a central probe channel, that the mitigated or enhanced XTs due to left- or right-hand side neighbor channels are averaged out.

2.6 Complete System Performance Considering All Transmission Impairments

In this section, we shall include all possible transmission impairments, in addition to the XPM-induced XT described in the last section. These impairments include receiver thermal noise, signal-spontaneous and spontaneous-spontaneous beat noise due to optical amplifiers, shot noise, and linear fiber dispersion induced nonlinear distortions (CSOs and CTBs which were discussed in Sec. 2.3). Note that in the 64 channels QPSK system example shown in Table 2.3, only CSOs need to be considered in the transmission system when OMI per channel is $\ll 1$ (this is because $\text{CSO} \sim m^2$ and $\text{CTB} \sim m^4$). However, if we consider a system with modulation frequencies distributed within an octave, e.g., 32-channel 155 Msps 16-QAM or QPSK equally distributed between 6.882 and 12.648 GHz, then only CTB needs to be considered. As we will see, keeping all modulation channels within an octave is a way to achieve high capacity, long distance transmission without dispersion compensation.

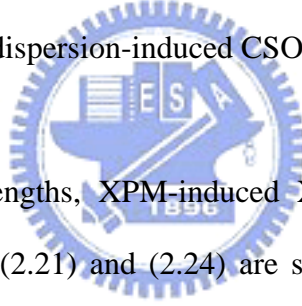


We used an EDFA pre-amplifier in the system so that the receiver thermal noise is not dominant [20]. The pre-amplifier has an unsaturated gain of 30 dB, a 3-dB saturation output power of 10 dBm, and a noise figure of 5 dB.

1) 64 channels of QPSK: Four wavelengths, each carrying the same 64-channel QPSK signals (see Table 2.3), are considered in an 80 km transmission system. No dispersion compensation is used. The probe wavelength again is λ_3 .

Fig. 2.10 shows the theoretical results of the worst-case noise-to-signal-ratio (NSR) (the worst among 64 subcarrier channels) as a function of *RMS OMI/ch*. Note that in the case of four wavelengths, the worst-case channel frequency depends on the combination of CSO and XPM-induced XT. The dashed line represents the NSR caused by linear fiber dispersion-induced CSOs, which was obtained from (2.12). It

shows that the NSR is proportional to the square of *RMS OMI/ch*. Due to this linear-dispersion-limited NSR, we must have a low *OMI/ch* in order to obtain a low NSR, e.g., *OMI/ch* less than 1.5% to obtain $\text{NSR} < -20 \text{ dB}$. However, to reach a long transmission distance with such a small *OMI/ch*, the launched optical power per wavelength has to be high. When there is only a single wavelength, we see from the three dotted lines in Fig. 2.10 that the launched optical power has to be as high as 10 dBm so that NSR can reach its best value of -20 dB to meet the requirement of a QPSK signal. We also notice that there is an optimum *OMI/ch*, i.e., 2.2%, 1.6%, and 1.1%, for the three power levels, respectively. When the *OMI/ch* is low, e.g., lower than 1%, the dominant noise is the signal-spontaneous beat noise, which is linearly proportional to the signal power. When the *OMI/ch* is high, e.g., higher than 2%, the dominant noise is the linear-dispersion-induced CSO.



In the case of four wavelengths, XPM-induced XT has to be included, and the theoretical results based on (2.21) and (2.24) are shown by solid lines in Fig. 2.10. Note that the wavelength separation is 50GHz, and the probe wavelength is at the center of the four wavelengths, i.e., λ_3 . As shown in (2.20), XPM-induced XT is proportional to the square of optical power per wavelength, thus a 10 dBm input power per wavelength causes a significant degradation to the single-wavelength NSR. When the input optical power is -2 dBm per wavelength, the theoretical results are the same for both single and four wavelengths. This is because the XPM-induced XT is negligible when compared to the combination of fiber dispersion-induced CSOs and signal-spontaneous beat noise. When the input power is 4 dBm per wavelength, the NSR is only slightly degraded by the XPM-induced XTs.

Fig. 2.11 shows the distribution of NSR in all the RF channels ($\text{OMI/ch} = 1.8\%$) given

in Table 2.3, when there are four equal-power wavelengths with per wavelength power of -2 , 4 , or 10 dBm and a channel spacing of 50 GHz. The theoretical results (dotted lines) are based on (2.12), (2.21), (2.24) and various receiver noise terms. Again, the NSR limited by the linear fiber dispersion-induced CSOs (see Eq.(2.12)) serves as the fundamental limitation of the given transmission system despite of the wavelength power level. We see from Fig. 2.11 that it is impossible for all QPSK channels to reach the minimum practical requirement of -20 dB NSR after 80 km of transmission without dispersion compensation, unless a forward error correction (FEC) coding gain is available.

Also shown in the figure are the simulation (circle) and numerical (solid line) results, which exhibit excellent agreement over the entire frequency range of the subcarrier channels for all optical powers. Theoretical results at 10 dBm, however, show slight discrepancy (~ 2 dB) from the simulation results. This is because the high-power-induced fiber nonlinearity affects the applicability of the linear-system IM-FTF, as was discussed in section 2.5.1. When the input power per wavelength is 4 dBm, we can see in Fig. 2.11 that the worst-channel NSR is about -16 dB, and is consistent with what was presented in Fig. 2.10.

Table 2.4 summarizes the theoretical results based on the optimum input optical power per wavelength, $RMS\ OMI/ch$ and the corresponding worst-case NSR for a wavelength spacing of 25 , 50 and 100 GHz, respectively. It can be seen that the wider the wavelength spacing, the higher input optical power per wavelength can be launched into the system, the lower OMI per channel can be used, and a better NSR performance can be obtained.

The coding gains required to reach a BER of 10^{-12} in practice for all wavelength spacings are also shown. These coding gains should be within the reach of conventional Reed-Solomon FEC codecs. For longer transmission distance, more optical amplifier-induced noise will have to be added (even though CSO is already close to its highest value, similar to what was shown in Fig. 2.5), and the coding gain may not be enough to cope with this additional noise due to longer transmission. Setting the total modulation bandwidth to within an octave may be a good solution to this problem. The following example confirms the feasibility of this approach.

2) 32 channels of 16-QAM or QPSK: Four wavelengths, each carrying 32-channel 155 Msps 16-QAM (or QPSK) signals equally distributed between 6.882 and 12.648 GHz, are considered in an 80 km transmission system. No dispersion compensation is used. The probe wavelength again is λ_3 .

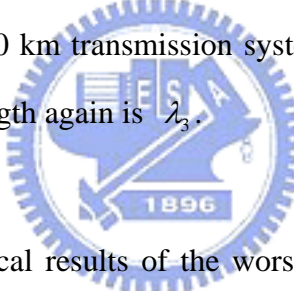


Fig. 2.12 shows the theoretical results of the worst-case NSR as a function of $RMS\ OMI/ch$. The dashed line represents the NSR caused by linear fiber dispersion-induced third order nonlinear distortions, which were obtained from (2.15). It shows that the NSR is proportional to m^4 . It is obvious that we can now work in a region with much higher OMI/ch than that in Fig. 2.10. To reach an $NSR < -27$ dB for practical 16-QAM signals without coding gain, OMI/ch needs to be less than 6.5%. When there is only a single wavelength, we see from the three dotted lines in Fig. 2.12 (for a launched power of -6, 0, and 6 dBm per wavelength) that the launched optical power has to be as high as 6 dBm such that NSR can reach its best value of -29 dB to meet the requirement of a 16-QAM signal. We also notice that there is an optimum OMI/ch , i.e., 7.1%, 5.6%, and 4.5%, for the three power levels, respectively. When the OMI/ch is low, e.g., lower than 4%, the dominant noise is the signal-spontaneous

beat noise, which is linearly proportional to the signal power. When the OMI/ch is high, e.g., higher than 7%, the dominant noise is the linear-dispersion-induced CTB.

In the case of four wavelengths, XPM-induced XT is included, and the theoretical results based on (2.21) and (2.24) are shown by solid lines in Fig. 2.12. We can observe: (1) when the input optical power is as low as -6dBm per wavelength, the theoretical results are the same for both cases of single and four wavelengths, because the XPM-induced XT is negligible; (2) when the input optical power is as high as 6 dBm per wavelength, the XPM-induced XT degrades the single-wavelength NSR severely; and (3) when the input power is 0 dBm per wavelength, the NSR is only slightly degraded by the XPM-induced XTs.

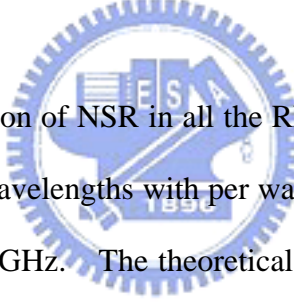


Fig. 2.13 shows the distribution of NSR in all the RF channels ($OMI/ch= 5.5\%$), when there are four equal-power wavelengths with per wavelength power of -6, 0, or 6 dBm and a channel spacing of 50 GHz. The theoretical results (dotted lines) are based on (2.15), (2.21), (2.24) and additive receiver noise terms. The NSR limited by the linear fiber dispersion-induced CTBs (see Eq.(2.15)) serves as the fundamental limitation of the transmission system, which gives a NSR limit of about -30 dB after 80 km transmission. If we carefully choose 0 dBm as the per wavelength power level to avoid XPM-induced XT, the resultant NSR is about -24 dB and is limited by the amplifier signal-spontaneous beat noise. This NSR is more than sufficient for QPSK signals, but requires > 3 dB FEC gain for 16-QAM signals.

Also shown in the figure are the simulation (circle) and numerical (solid line) results, which exhibit excellent agreement over the entire frequency range of the subcarrier channels for all optical powers. Theoretical results at 6 dBm, however, show slight

discrepancy (~ 1 dB) from the simulation results because of the accuracy of the theoretical prediction of XPM-induced XT due to high-power-induced fiber nonlinearity. When the input power per wavelength is 0 dBm, we can see in Fig. 2.13 that the worst-channel NSR is about -24 dB, and is consistent with what was presented in Fig. 2.12.

Table 2.5 summarizes the theoretical results based on optimum input optical power per wavelength, $RMS\ OMI/ch$ and the corresponding worst-case NSR for a wavelength spacing of 25, 50 and 100 GHz, respectively. It can be seen that the wider the wavelength spacing, the higher input optical power per wavelength can be launched into the system, the lower OMI/ch can be used, and a better NSR performance can be obtained. Also note that the worst-channel NSR can get 7.7 to 8.5 dB improvement than those given in Table 2.4. This implies that we can comfortably increase the constellation to 16-QAM, while maintaining the same system capacity (20 Gbps) and transmission distance. On the other hand, if we decrease the transmission capacity to 10 Gbps by using 32 channels of 155 Msps QPSK within an octave, we can obtain a much longer transmission distance than 80 km because now the main system limitation comes from amplifier signal-spontaneous beat noise, just as in conventional transmission systems.

2.7 Summary

We have investigated the fundamental linear and nonlinear system limitations of multi-channel SSB/SCM/DWDM systems through theoretical analysis, numerical calculations, and computer simulations. We have presented general analytical tools which can be used in either wireless or metro optical systems which transport multiple SSB/SCM

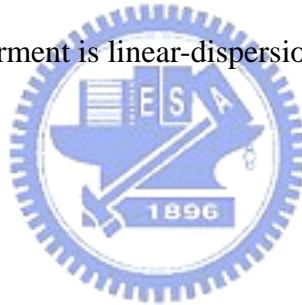
narrowband digital signals on a single or multiple wavelengths. These analytical tools include: Eq.(2.11) and Table 2.1 for MZI modulator-induced CTB; Eq.(2.12) and Table 2.2 for CSOs caused by linear fiber dispersion; Eqs.(2.13)-(2.15) for CTBs caused by linear fiber dispersion; Eqs. (2.21)-(2.24) for XPM-induced XT. To predict XPM-induced XT precisely and without the limitation of wavelength spacing or modulation frequency range, Eq.(2.20) was derived for numerical calculations.

Through case studies of 64 or 32 channels of 155 Msps n-QAM signals, we discovered the following system considerations for SSB/SCM/DWDM transmissions:

- (1) The MZI modulator nonlinear transfer curve-induced CTB is the very basic SSB/SCM system limitation even when all fiber dispersion has been completely compensated. This CTB is usually not of concern because it is relatively low, e.g., lower than -30 dBc (64 channels) and -50 dBc (32 channels) in our case studies.
- (2) Although an SSB/SCM system does not have the same distance-dependent carrier suppression problem as in a conventional double-sided SCM system, its transmission distance is still severely limited by linear fiber dispersion-induced CSOs when the multiple modulation signals occupy more than an octave of frequency range. In our case study of 64 channels of QPSK signals with 4% *OMI/ch*, this CSO can be as high as -17 dBc and -9 dBc when the transmission distances are ~ 50 and > 150 km, respectively. Beyond 150 km, this CSO saturates at -9 dBc.
- (3) The main optical fiber nonlinearity-induced impairment in a DWDM SSB/SCM system is caused by XPM. To avoid this XPM-induced XT, the launched optical power per wavelength should be kept below a certain level

(about 3 dBm in our case studies).

- (4) Two case studies of 20 Gbps per wavelength over an 80 km DWDM system without dispersion compensation were carried out. We found that both are theoretically achievable but with little margin left, especially when wavelength channel spacing is small. We did notice that, however, it is possible to transport 10 Gbps (e.g., 32 155 Msps QPSK signals with traditional FEC and within an octave) per wavelength using SSB/SCM in a DWDM system, even at 25 GHz wavelength spacing, over a transmission distance of many hundreds of kilometers without dispersion compensation. The key point in achieving this superior transmission performance is to keep all the modulation frequencies within an octave so that the dominant transmission impairment is linear-dispersion-induced CTB.



Chapter 3 An Evolutionary HFC Network

Architecture for Adding Narrowcast Services

Using dense-wavelength-division-multiplexing (DWDM) technology to deliver both broadcast and narrowcast services in hybrid-fiber-coax (HFC) systems has recently attracted significant interest. The typical 64/256 quadrature amplitude modulated (QAM) channel loading on each ITU-grid wavelength of today's commercial product is only 8~16 channels. The main reason why higher number of channel loading is difficult is because the broadcast and narrowcast channels can interfere with each other at the single-photodiode receiver [21]. Furthermore, most of the proposed DWDM-system based HFC architecture uses a dedicated wavelength for a single optical node [21], [22]. Consequently, only 8~16 QAM channels are delivered to an optical node. This makes future upgrade to higher number of QAM channels (to accommodate more and more digital video and video-on-demand channels) per optical node a difficult task.



On the other hand, some optical nodes may require only a few QAM channels in the beginning stage. For example, if the narrowcast targeted services include only Internet access, packet telephony, teleconferencing, etc., only 4 ~ 5 64-QAM channels are required to cover all downstream narrowcast traffic for an optical node with a coverage size of 500 homes [23], [24]. Therefore, following previously proposed HFC architecture [21], [22] for adding narrowcast services to broadcast services, we find it very wasteful to use a dedicated wavelength for a particular optical node. This is especially true at the initial stage of delivering narrowcast services.

Considering the above two aspects, we see the need of an evolutionary HFC architecture

which can add narrowcast services gracefully while in the same time can be upgraded to provide a very large narrowcast transport capacity. Therefore, in this chapter we propose and experimentally verify a new HFC architecture in which only a single laser is used initially to *broadcast* multiple “narrowcast” M-QAM-carried digital services to multiple optical nodes. Although each subscriber can then receive all M-QAM channels, information intended for other subscribers cannot be eavesdropped owing to the data transport security protections defined in Data-Over-Cable Service Interface Specifications (DOCSIS) [25]. The proposed new HFC architecture can gracefully and economically meet the demands of HFC networks with both light and heavy downstream traffic.

3.1 Architectural Concept

The proposed architecture is shown in Fig. 3.1. In the beginning stage of providing narrowcast services, if the traffic demand is light, we can use only a single ITU-grid “narrowcast laser” ($\lambda_{NC,1}$) to broadcast multiple M-QAM channels to multiple optical nodes. For example, a “narrowcast laser” in the primary hub transports 50 channels of 64-QAM signals in the frequency range of 450 - 750 MHz (or 550 - 850 MHz), through a long transmission distance and reaches a secondary hub. The light power is then split M ways to M optical nodes.

Note that in this architecture, we propose using two optical fibers from the secondary hub to each optical node, and avoid using an optical coupler or a dual-wavelength WDM multiplexer to combine the “broadcast” laser (λ_{BC}) with $\lambda_{NC,1}$ into a single fiber. There are two reasons why we should use two optical fibers to each optical node. The main reason is because when we use two fibers and dual-receivers at the optical node, the dynamic range and the channel loading per narrowcast laser can be significantly increased [21], [24]. The

second reason is because the return-path signal can potentially utilize the narrowcast fiber via a dual-wavelength WDM multiplexer (e.g., a 1310/1550 nm multiplexer).

In the middle stage of network evolution, we can decrease the number of optical nodes that $\lambda_{NC,1}$ serves, and add a second ITU-grid narrowcast laser at $\lambda_{NC,2}$ to serve the rest of optical nodes. Multi-wavelength DWDM multiplexer and demultiplexer can be added at this stage. In the later stage of network evolution, we can add more and more narrowcast lasers (up to $\lambda_{NC,M}$), and eventually reaches the final architecture as what has been proposed today [21], [22]. During the evolutionary stages, it is clear that part of the nodes received $\lambda_{NC,1}$ as the narrowcast wavelength in the beginning stage, then received $\lambda_{NC,2}$ in the second stage, etc. We can see that the network evolution is extremely smooth considering the initial narrowcast demand and the lower cost involved. Another important advantage of this network architecture is that, when the final evolution stage is reached, each node can enjoy a narrowcast wavelength with a capacity of up to 50 QAM channels, instead of just 8 QAM channels as in today's HFC-DWDM commercial products.

3.2 Experiment and Analysis

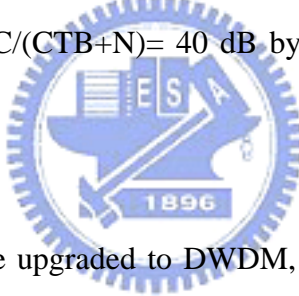
Our experimental setup for the long-distance narrowcast system is exactly the same as what is arranged for the transmission of $\lambda_{NC,1}$ in Fig. 3.1 (before upgrade to DWDM). An ITU-grid narrowcast MQW-DFB laser at 1553.3 nm was used. At a bias current of 52 mA, its output power, relative intensity noise (RIN), 3-dB bandwidth, and frequency chirp were 9 dBm, -165 dB/Hz, 3 GHz and 250 MHz/mA, respectively. 50 channels of CW tones, simulating 50 channels of M-QAM signal [5], were used to directly modulate the laser. A booster EDFA with an output power of +19 dBm and a noise figure of 6 dB was used. Following the booster EDFA were a 3 dB pad, 81 km of conventional single mode fiber

(SMF), and an in-line EDFA with a noise figure of 5 dB. The input and output power levels of the in-line EDFA were 0 and 19 dBm, respectively. Following the in-line EDFA were 14 dB attenuation, 21.5 km of SMF, and a conventional CATV optical receiver. The 14 dB optical attenuation is equivalent to the power loss due to a typical 1×16 optical splitter.

There are three factors that need to be considered in choosing the optimum optical modulation index per channel (OMI/ch): (1) minimizing the stimulated Brillouin scattering (SBS)-induced nonlinear distortions; (2) minimizing the double Rayleigh backscattering (DRB)-induced intensity noise; and (3) minimizing the fiber dispersion-induced nonlinear distortions. Since our architecture uses a dedicated optical receiver for the narrowcast M-QAM signals within an octave, the second-order nonlinear distortions (NLDs) are not of concern. The second-order NLDs can be eliminated by the diplex filter located after the dual optical receivers to avoid degrading the broadcast signal quality. Therefore, we only have to concentrate on the composite triple beat (CTB) products caused by the 50 CW tones, and the carrier-to-noise-ratio (CNR) per channel. In considering factor (1), our measured results of SBS threshold (defined as the launched optical power at which the backward Stokes power is lower than -25 dB of the launched power) as a function of the *OMI/ch* are plotted in Fig. 3.2. We see that as long as the OMI/ch is greater than about 1.7%, our launched power from the booster EDFA (with a 3 dB pad) can always be below the SBS threshold of +16dBm.

In considering factors (2) and (3), Fig. 3.3 shows the measured (solid circles) and calculated (dashed line) worst-case C/CTB after 100 km of transmission as a function of *OMI/ch*. The dashed line is the calculated results base on a closed-form analysis [22], which shows that C/CTB decreases with fourth power of *OMI/ch*. On the other hand, when OMI/ch is

smaller than about 3%, DRB-induced intensity noise became dominant, as can also be theoretically predicted (solid line) [27]. Consequently, we see that carrier-to-(CTB + total noise), i.e. $C/(CTB+N)$, drops for $OMI/ch < 3\%$. We therefore picked an optimum OMI/ch at 3.1% for system operation. By using this OMI/ch , the received RF spectrum after 102.5 km SMF and 14 dB attenuation is shown in Fig. 3.4. We can clearly see the fiber-dispersion-induced second-order NLDs at lower frequency range, and the worst-case CTB (-42.5 dBc) from the zoomed-in spectrum. The C/CTB and $C/(CTB+N)$ for all of the received 50 channels (from 450 to 750 MHz) are shown in Fig. 3.5. We can see that C/CTB and $C/(CTB+N)$ differ by ~ 4 dB, which indicates that the CTB level and the noise level were about equal. The resultant $C/(CTB+N)$ of the worst-case channel was around 39 dB, which is one dB less than the industry specification [28]. We believe that it is possible to achieve the required $C/(CTB+N)= 40$ dB by reducing the transmission length from 102.5 to 90 km.



Since the network will have to be upgraded to DWDM, we need to understand how fiber nonlinearities could affect the performance of the proposed architecture. Therefore, we used a 4-wavelength setup shown in Fig. 3.6 to measure the crosstalk levels among DWDM channels for a transmission distance of 80 km. The probe wavelength channel, which is the right-most channel in the optical spectrum at the output of the DWDM EDFA, was operated under CW while each of the other three lasers was modulated by a RF frequency synthesizer. The launched optical power of the probe channel was controlled to be less than 6 dBm to avoid SBS effect, while the launched optical power of the other three lasers were at +10 dBm per wavelength. At the receiver end, the probe wavelength channel is extracted by using a tunable optical filter for crosstalk measurement. Three polarization controllers were used to obtain the worst-case crosstalk.

Fig. 3.7 shows the measured and analytical crosstalk [4] results as a function of RF frequency. Since the analytical results match fairly well with measured results, we can analytically predict (solid line in Fig. 3.7) that the worst-case crosstalk of the four-3.2 nm-spacing-wavelengths, after 80 km of transmission would be less than -44 dBc.

If the transmission distance from the secondary hub to fiber nodes is fixed at 20 km, Fig. 3.8 shows the calculated maximum transmission distance between primary and secondary hub versus wavelength spacing for 4, 8 and 16 wavelengths, for $C/(CTB+N+XT) = 40$ dB on the received 64-QAM channel. We can see that the maximum transmission distance between primary and secondary hub can be more than about 49 km. The coverage size from primary hub to fiber nodes is consequently about 70 km.

3.3 Summary



We have experimentally verified the feasibility of a proposed HFC network architecture. This architecture incorporates a smooth transition from a single-wavelength narrowcast laser to DWDM narrowcast lasers. For a 64-QAM channel loading of 50 per wavelength, and using dual-receiver fiber nodes, the coverage range can be up to ~ 100 km when using a single laser, and can be up to ~ 70 km when using 16 wavelengths. Therefore, this architecture can meet the demand of an HFC network economically and gracefully with both light and heavy narrowcast traffic demands.

Chapter 4 Conclusions

In the thesis, we investigated the fundamental linear and nonlinear system limitations of multichannel SSB/SCM/DWDM systems through theoretical analysis, numerical calculations, and computer simulations. We have presented general analytical tools, which can be used in either wireless or metro optical systems, which transport multiple SSB/SCM narrowband digital signals on a single or multiple wavelengths. These analytical tools include: (2.11) and Table 2.1 for MZI modulator-induced CTB; (2.12) and Table 2.2 for CSOs caused by linear fiber dispersion; (2.13) – (2.15) for CTBs caused by linear fiber dispersion; (2.21) – (2.24) for XPM-induced XT. To predict XPM-induced XT precisely and without the limitation of wavelength spacing or modulation frequency range, (2.20) was derived for numerical calculations.

Through case studies of 64 or 32 channels of 155 Msymbol/s n-QAM signals, several system considerations for SSB/SCM/DWDM transmission were discovered.

- The MZI modulator nonlinear transfer curve-induced CTB is the very basic SSB/SCM system limitation even when all fiber dispersion has been completely compensated.
- Although an SSB/SCM system does not have the same distance-dependent carrier suppression problem as in a conventional double-sided SCM system, its transmission distance is still severely limited by linear fiber dispersion-induced CSOs when the multiple modulation signals occupy more than an octave of frequency range.
- The main optical fiber nonlinearity-induced impairment in a DWDM SSB/SCM system is caused by XPM. To avoid this XPM-induced XT, the launched optical power per wavelength should be kept below a certain level.
- Two case studies of 20 Gb/s per wavelength over an 80 km DWDM system

without dispersion compensation were carried out. We found that both are theoretically achievable but with little margin left, especially when wavelength channel spacing is small. We did notice that, however, it is possible to transport 10 Gb/s (e.g., 32-ch 155 Msymbol/s QPSK signals with traditional FEC and within an octave) per wavelength using SSB/SCM in a DWDM system, even at 25-GHz wavelength spacing, over a transmission distance of many hundreds of kilometers without dispersion compensation. The key point in achieving this superior transmission performance is to keep all the modulation frequencies within an octave so that the dominant transmission impairment is linear-dispersion-induced CTB.

We also proposed a new HFC network architecture in the thesis, whose feasibility has been experimentally verified. This architecture incorporates a smooth transition from a single-wavelength narrowcast laser to DWDM narrowcast lasers. For a 64-QAM channel loading of 50 per wavelength, and using dual-receiver fiber nodes, the coverage range can be up to \sim 100 km when using a single laser, and can be up to \sim 70 km when using 16 wavelengths. Therefore, this architecture can meet the demand of an HFC network economically and gracefully with both light and heavy narrowcast traffic demands.

References

- [1] G. H. Smith, D. Novak, and Z. Ahmed, “Technique for optical SSB generation to overcome dispersion penalties in fiber-radio systems,” *Electron. Lett.*, vol.33, pp.74–75, Jan. 1997.
- [2] G. H. Smith and D. Novak, “Broad-band millimeter-wave (38 GHz) fiber-wireless transmission system using electrical and optical SSB modulation to overcome dispersion effects,” *IEEE Photon. Technol. Lett.*, vol. 10, pp. 141–143, Jan. 1998.
- [3] F. Ramos and J. Marti, “Comparison of optical single-sideband modulation and chirped fiber gratings as dispersion mitigating techniques in optical millimeter-wave multichannel systems,” *IEEE Photon. Technol. Lett.*, vol. 11, pp. 1479–1481, Nov. 1999.
- [4] M. R. Phillips and D. M. Ott, “Crosstalk due to optical fiber nonlinearities in WDM CATV lightwave systems,” *J. Lightwave Technol.*, vol. 17, no. 10, pp. 1782–1792, Oct. 1999.
- [5] Ming-Chia Wu, Pi-Yang Chiang and Winston I. Way, “On the validity of using CW tones to test the linearity of multichannel M-QAM subcarrier multiplexed lightwave systems,” *IEEE Photon. Technol. Lett.*, vol. 12, no. 4, pp. 413–415, April 2000.
- [6] H. Schmuck, “Comparison of optical millimetre-wave system concepts with regard to chromatic dispersion,” *Electron. Lett.*, vol. 31, no.21, pp. 1848–1849, Oct. 1995.
- [7] A. Cartaxo, “Impact of modulation frequency on cross-phase modulation effect in intensity modulation-direct detection WDM systems,” *IEEE Photon. Technol. Lett.*, vol. 10, pp. 1268–1270, Sept. 1998.
- [8] A. Cartaxo, “Cross-phase modulation in intensity Modulation-direct Detection WDM systems with multiple optical amplifiers and dispersion compensators,” *J. Lightwave Technol.*, vol. 17, no. 2, pp. 178–190, Feb. 1999.

- [9] J. Wang and K. Petermann, “Small signal analysis for dispersive optical fiber communication systems,” *J. Lightwave Technol.*, vol. 10, no. 1, pp. 96–100, Jan. 1992.
- [10] A. Røyset, L. Bjerkan, D. Myhre and L. Hafskjær, “Use of dispersive optical fiber in the characterization of chirp in semiconductor lasers,” *Electron. Lett.*, vol. 30, no.9, pp. 710–712, April 1994.
- [11] L. Bjerkan, A. Røyset, L. Hafskjær and D. Myhre, “Measurement of laser parameters for simulation of high-speed fiberoptic systems,” *J. Lightwave Technol.*, vol. 14, pp. 839–850, May. 1996.
- [12] A. Røyset, L. Bjerkan and A. Sudb, “Compensation of optical fiber dispersion in the electrical domain for transmission systems with direct detection,” *Electron. Lett.*, vol. 30, no.2, pp. 152–153, Jan. 1994.
- [13] A. Cartaxo, B. Wedding and W. Idler, “Influence of fiber nonlinearity on the fiber transfer function: theoretical and experimental analysis,” *J. Lightwave Technol.*, vol. 17, no. 10, pp. 1806–1813, Oct. 1999.
- [14] F. Ramos and J. Marti, “Frequency transfer function of dispersive and nonlinear single-mode optical fibers in microwave optical systems,” *IEEE Photon. Technol. Lett.*, vol. 12, no. 5, pp.549–551, May. 2000.
- [15] F. Devaux, Y. Sorel, and J. Kerdiles, “Simple measurement of fiber dispersion and of chirp parameter of intensity modulated light emitter,” *J. Lightwave Technol.*, vol. 11, pp. 1937–1940, Dec. 1993.
- [16] A. Cartaxo, B. Wedding, and W. Idler, “Influence of fiber nonlinearity on the phase noise to intensity noise conversion in fiber transmission: theoretical and experimental analysis,” *J. Lightwave Technol.*, vol. 16, pp. 1187–1194, July. 1998.
- [17] G. P. Agrawal, *Nonlinear Fiber Optics*, 2nd ed. San Diego, CA:Academic, 1995.
- [18] T. K Chiang, N. Kagi, M. E. Marhic and L. G. Kazovsky, “Cross-phase modulation in

fiber links with multiple optical amplifiers and dispersion compensators,” *J. Lightwave Technol.*, vol. 14, pp. 249–260, Mar. 1996.

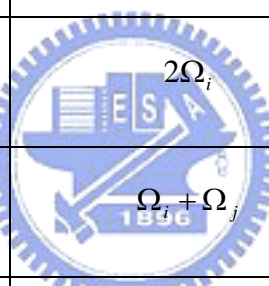
- [19] P. Laurêncio and M. C. R. Medeiros, “Dynamic range of optical links employing optical single side-band modulation,” *IEEE Photon. Technol. Lett.*, vol. 15, no. 5, pp. 748–750, May. 2003.
- [20] W. I. Way, *Broadband Hybrid Fiber/Coax Access System Technologies*, Academic Press, New York, 1998.
- [21] V. Mutualik, “DWDM-making the best fit,” CED Magazine, pp. 38-50, Sept. 1999.
- [22] S. Mysore, “Twenty-wavelength, dual-receiver DWDM system: modeling and experiments,” Technical Digest, IEEE LEOS Summer Topical Meeting, pp. 5-6, paper WC2.3, July 1999.
- [23] D. Pike and T. E. Werner, Technical Papers, “On plant renewal strategies,” Technical Papers, NCTA, pp. 217-245, May 1998.
- [24] W. H. Chen, J. K. Wong and W. I. Way, “Experimental verification of an evolutionary HFC network architecture for adding narrowcast services,” in OFC2000 Technical Digest, pp. 157-159, paper WJ5.
- [25] DOCSIS Baseline Privacy Plus Interface Specification. SP-BPI+-I01-990316.
- [26] D. B. Crosby and G. J. Lampard, “Dispersion-induced limit on the range of octave confined optical SCM transmission systems,” *IEEE Photon. Technol. Lett.*, vol. 6, no. 8, pp. 1043–1045, Aug. 1994.
- [27] P. Wan and J. Conradi, “Impact of double Rayleigh backscatter noise on digital and analog fiber systems,” *J. Lightwave Technol.*, vol. 14, no. 3, pp. 288–297, Mar. 1996.
- [28] O. J. Sniezko and T. E. Werner, “Invisible hub or end-to-end transparency,” Technical Papers, NCTA, pp. 247-257, May 1998.

Tables

Table 2.1 Analytic expressions for the individual third order distortions due to SSB/SCM Modulation, Ω_i , Ω_j and Ω_k , are three arbitrarily chosen distinct subcarrier frequencies.

Distortion Type	Distortion Frequency (Ω_d)	Formula
Third Harmonic	$3\Omega_i$	$\left[\frac{J_0(m)J_3(m) - J_1(m)J_2(m)}{J_0(m)J_1(m)} \right]^2$
Third-Order Intermodulation	$2\Omega_i \pm \Omega_j$	$\left[\frac{J_1(m)}{J_0(m)} \right]^4$
Triple Beat	$\Omega_i \pm \Omega_j \pm \Omega_k$	$4 \cdot \left[\frac{J_1(m)}{J_0(m)} \right]^4$

Table 2.2 Analytic expressions for SSB/SCM 2nd order NLDs due to linear fiber dispersion. $\rho = 1/2 \cdot \beta_2 \cdot z$.

Distortion Type	Distortion Frequency (Ω_d)	Formula
Second Harmonic	 $2\Omega_i$	$2 \left[\frac{J_2(m) \sin(\rho \cdot \Omega_d^2)}{J_1(m)} \right]^2$
2 nd order Intermodulation (IM_{i+j})	 $\Omega_i + \Omega_j$	$2 \left[\frac{J_1(m) \sin(\rho \cdot \Omega_d^2)}{J_0(m)} \right]^2$
2 nd order Intermodulation (IM_{i-j})	$\Omega_i - \Omega_j$	$2 \cdot \left[\frac{J_1(m)}{J_0(m)} \right]^2 \cdot C^*$

$$^*C = \left[\cos(\rho \cdot (\Omega_i^2 - \Omega_j^2)) - \cos(\rho \cdot \Omega_d^2) \right]^2 + \left[\sin(\rho \cdot (\Omega_i^2 - \Omega_j^2)) \right]^2$$

Table 2.3 Parameters for a 20 Gb/s SSB/SCM systems

Number of subcarrier channels on pump wavelength	64
Bandwidth Efficient Modulation (BEM) scheme	QPSK
Symbol rate per channel	155 Msymbol/s
Bandwidth excess factor	0.2
Channel spacing	1.2×155 MHz
Channel frequency plan	0.93 ~ 12.648 GHz
Optical modulation scheme	USB/SCM
Number of wavelengths	2 (Fig. 2.8), 4 (Fig. 2.9–Fig. 2.13)
Wavelength separation	25, 50, and 100 GHz
Probe Wavelength (λ_3)	1550 nm
Fiber dispersion coefficient at λ_3 (D)	17 ps/nm/km
Fiber dispersion slope at λ_3 (S)	0.044 ps/nm ² /km
Fiber nonlinear index coefficient (n_2)	$2.6 \times 10^{-20} \text{ m}^2/\text{W}$
Fiber effective core area (A_{eff})	$80 \mu\text{m}^2$
Fiber nonlinearity coefficient at λ_3 ($\gamma = 2\pi n_2 / \lambda A_{eff}$)	$1.32 \text{ W}^{-1}\text{km}^{-1}$
Fiber power attenuation coefficient (α)	0.21 dB/km
Fiber length	80 km
Receiver equivalent thermal noise	$10 \text{ pA}/\sqrt{\text{Hz}}$

Table 2.4 For the system given in Table 2.3, a summary of the optimum optical power, *RMS OMI/ch* and the corresponding worst-case NSR in a transmission system with four multiplexed wavelengths. Three wavelength spacings are given: 25, 50 and 100 GHz. The required coding gains to reach a BER of 10^{-12} are also shown.

	25 GHz (0.2 nm)	50 GHz (0.4 nm)	100 GHz (0.8 nm)
Optimum optical power per wavelength (dBm)	2.24	4.48	6.81
Optimum RMS OMI per channel (%)	1.78	1.55	1.36
Worst-channel NSR (dB)	-14.66	-15.72	-16.88
Coding gain required to reach $\text{BER} = 10^{-12}$ (dB) in practice*	5.34	4.28	3.12

* For QPSK, $\text{NSR} < \sim -16.95 \text{ dB}$ in theory and -20 dB in practice is required to obtain a $\text{BER} = 10^{-12}$

Table 2.5 For 32 channels of 16-QAM signals equally distributed between 6.882 and 12.648 GHz (same transport capacity as that given in Table 2.3), a summary of the optimum optical power, RMS OMI/ch and the corresponding worst-case NSR in a transmission system with four multiplexed wavelengths. Three wavelength spacings are studied: 25, 50 and 100 GHz. The required coding gains to reach a BER of 10^{-12} for QPSK and 16-QAM are also shown.

	25 GHz (0.2 nm)	50 GHz (0.4 nm)	100 GHz (0.8 nm)
Optimum optical power per wavelength (dBm)	-1.49	0.75	3.01
Optimum RMS OMI per channel (%)	5.94	5.45	5
Worst-channel NSR (dB)	-22.39	-23.88	-25.39
Coding gain required to reach $\text{BER} = 10^{-12}$ (dB)* for QPSK	0	0	0
Coding gain required to reach $\text{BER} = 10^{-12}$ (dB)** for 16-QAM	4.61	3.12	1.61

* For QPSK, $\text{NSR} < \sim -16.95 \text{ dB}$ in theory and -20 dB in practice is required to obtain a $\text{BER} = 10^{-12}$

** For 16-QAM, $\text{NSR} < \sim -23.88 \text{ dB}$ in theory and -27 dB in practice is required to obtain $\text{BER} = 10^{-12}$

Figures

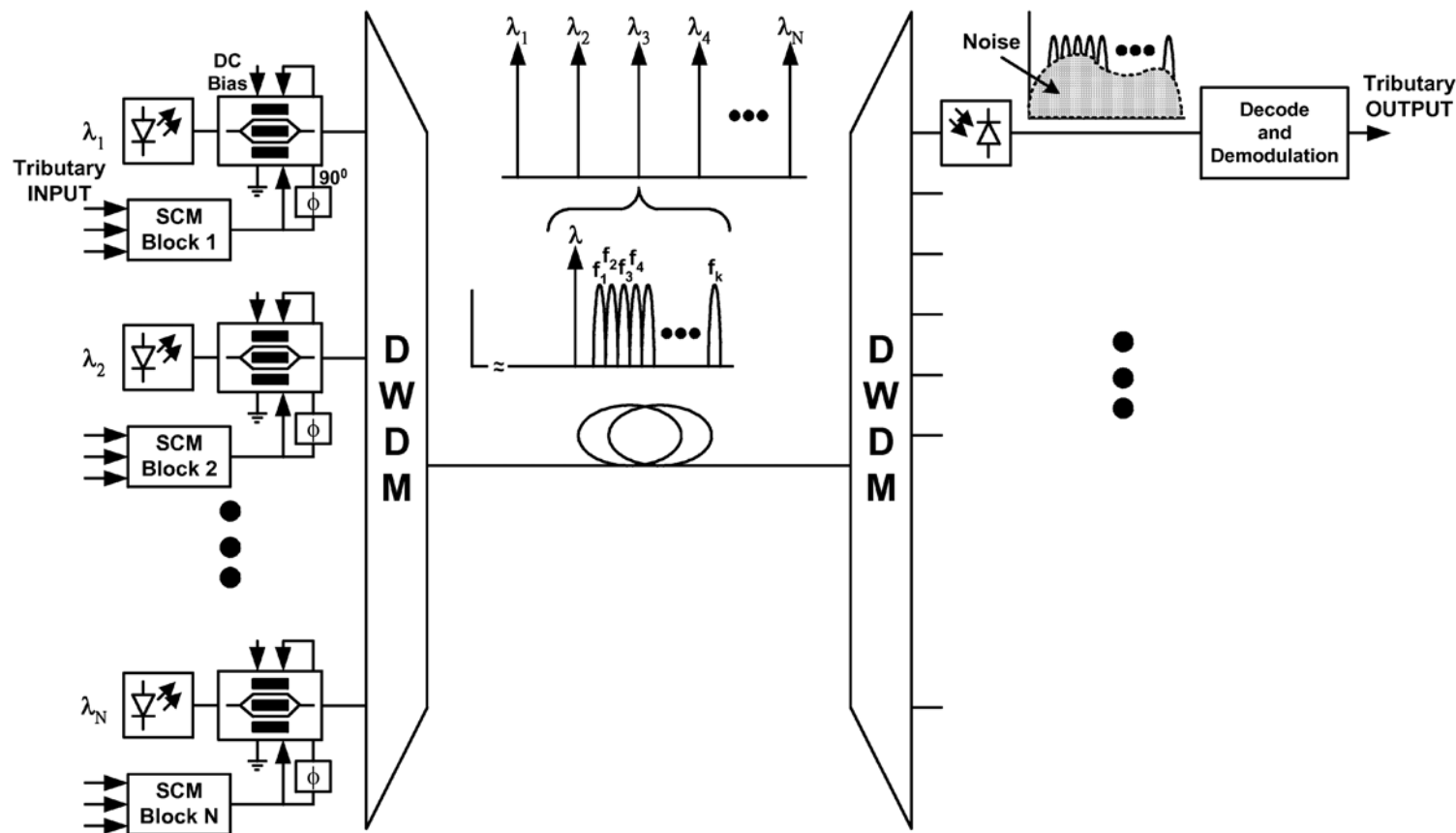


Fig. 2.1 An SSB/SCM/DWDM system.

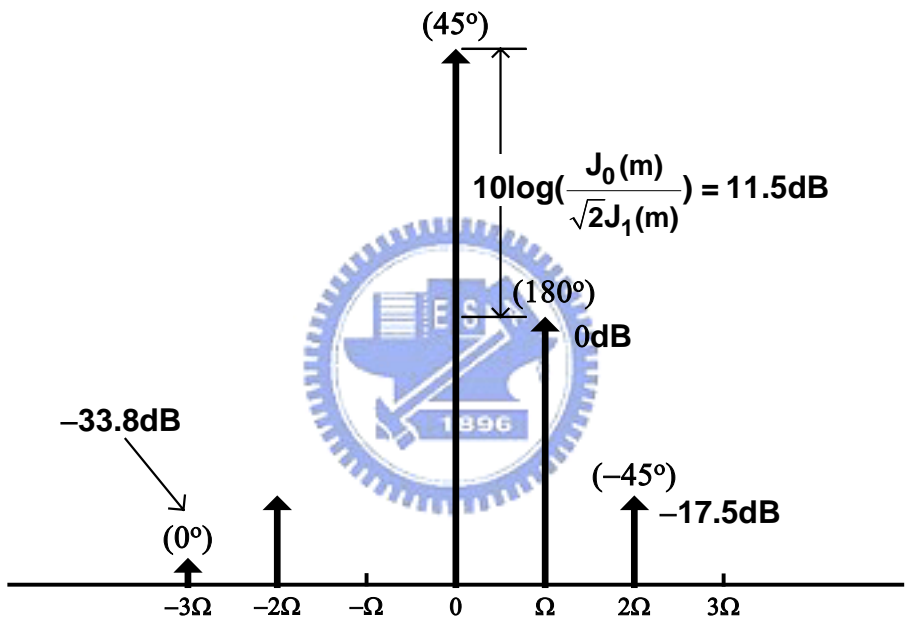


Fig. 2.2 Optical spectrum of a single channel SSB/SCM signal with $m=0.1$ (note that ω_0 is subtracted from all frequency components).

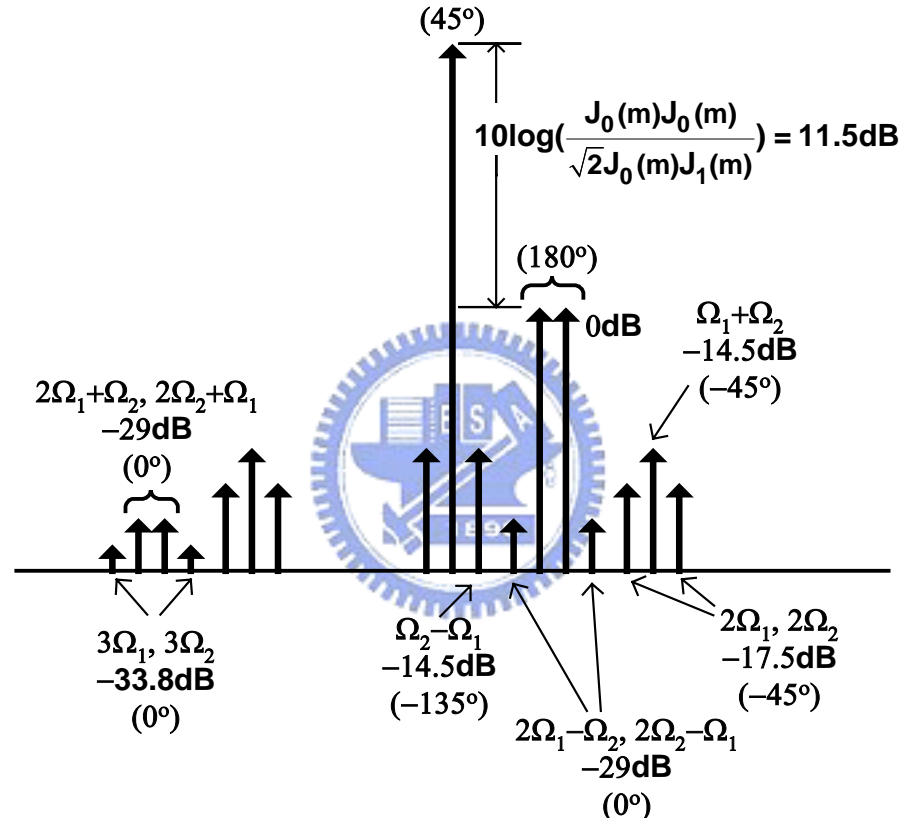


Fig. 2.3 Optical spectrum of a 2-ch SSB/SCM signal with $m=0.1$ (note that ω_0 is subtracted from all frequency components).

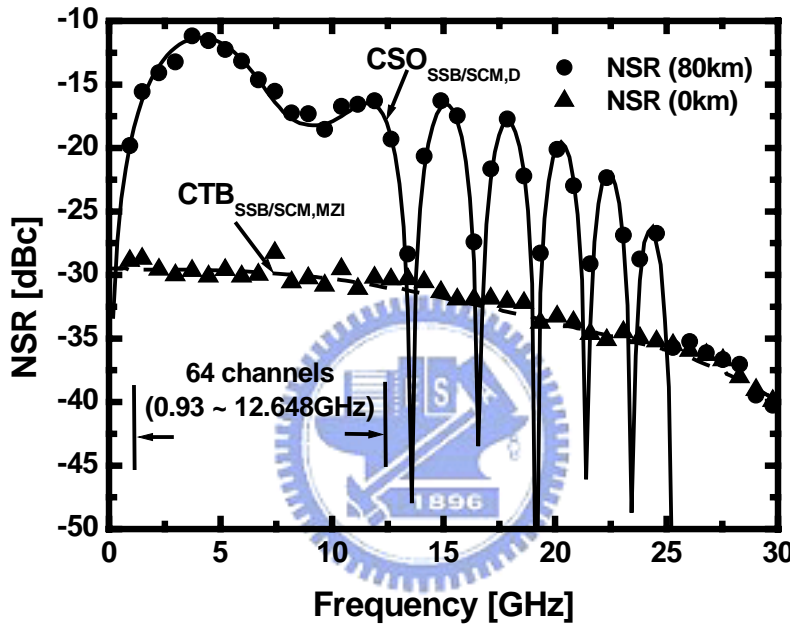


Fig. 2.4 Noise-to-signal ratio (NSR) versus frequency in an SSB/SCM optical transmission system with 64 QPSK channels (ranging from 0.93 to 12.648 GHz), for fiber lengths of 0 and 80 km. Dashed line and upper triangular symbols are the theoretical and simulation results for the case of no fiber transmission, respectively. Solid lines and circular symbols are the theoretical and simulation results after 80 km fiber transmission, respectively. RMS OMI per channel is around 4%.

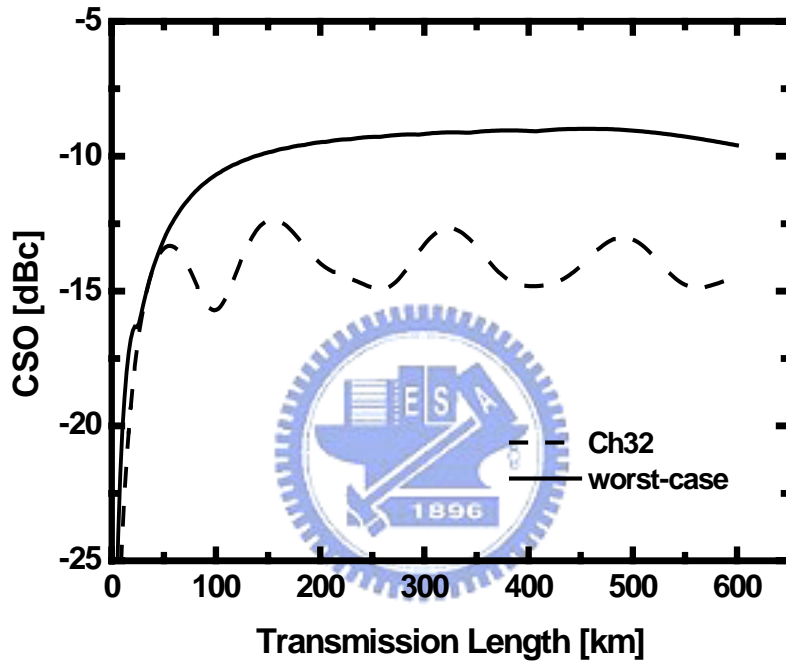


Fig. 2.5 Linear fiber dispersion-induced CSO versus transmission distance in a SSB/SCM system with 64 QPSK channels. Dashed and solid lines are the results of channel 32 and worst-case channel, respectively. RMS OMNI per channel is 4%.

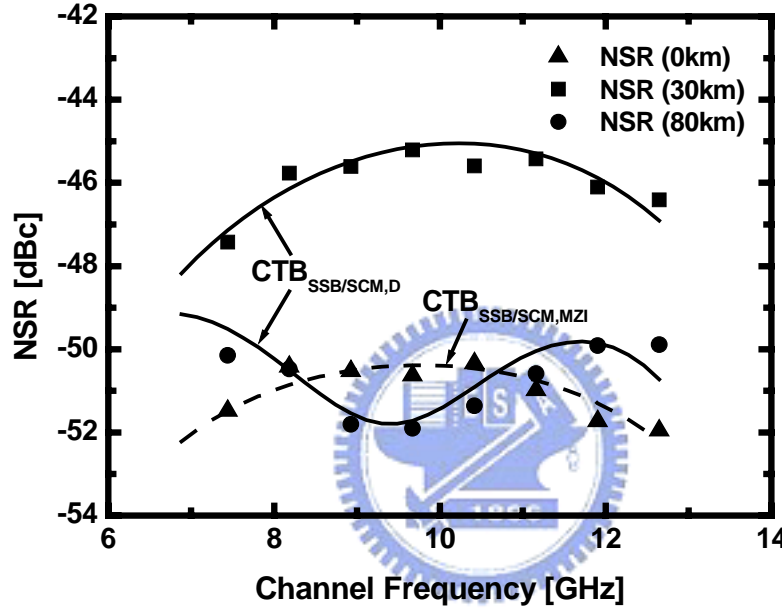


Fig. 2.6 Noise-to-signal ratio (NSR) versus frequency in an SSB/SCM optical transmission system with 32 16-QAM channels (ranged from 6.882 to 12.648 GHz), for fiber lengths of 0, 30 and 80 km. Dashed line and upper triangular symbols are the theoretical and simulation results for the case of no fiber transmission, respectively. Square and circle symbols are the simulation results after 30 and 80km fiber transmissions, respectively. Solid lines are the theoretical results. RMS OMIs per channel is around 1.8%.

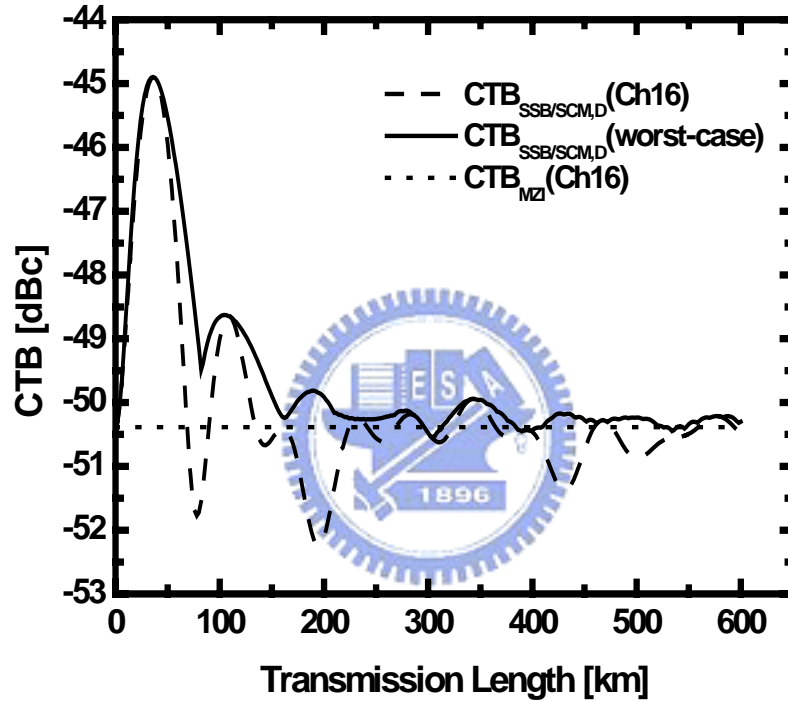


Fig. 2.7 Linear fiber dispersion-induced CTB versus transmission distance in an SSB/SCM system with 32 16-QAM channels. Dashed and solid lines are the results of channel 16 and worst-case channel, respectively. Dotted line is the intrinsic MZI-induced CTB at channel 16. RMS OMI per channel is 1.8%.

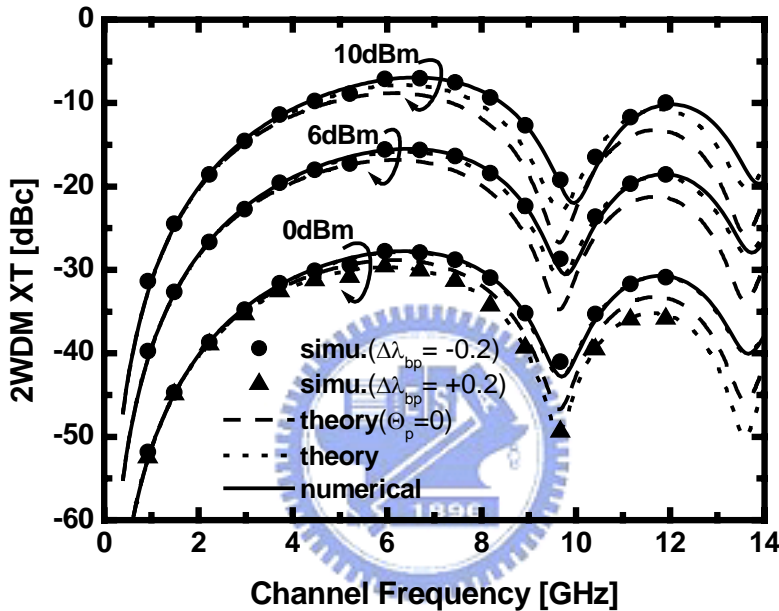


Fig. 2.8 Two wavelengths XT versus pump modulation frequency for an average optical power per wavelength of 0, 6 or 10 dBm. Circular ($\Delta\lambda_{bp} = -0.2$ nm) and triangular ($\Delta\lambda_{bp} = +0.2$ nm) symbols are simulation results; dashed ($\Theta_p = 0$) and dotted ($\Theta_p \neq 0$) lines show the theoretical predictions; solid lines are numerical results. The pump wave is modulated with 64 QPSK channels between 0.93 and 12.648 GHz using USB/SCM.

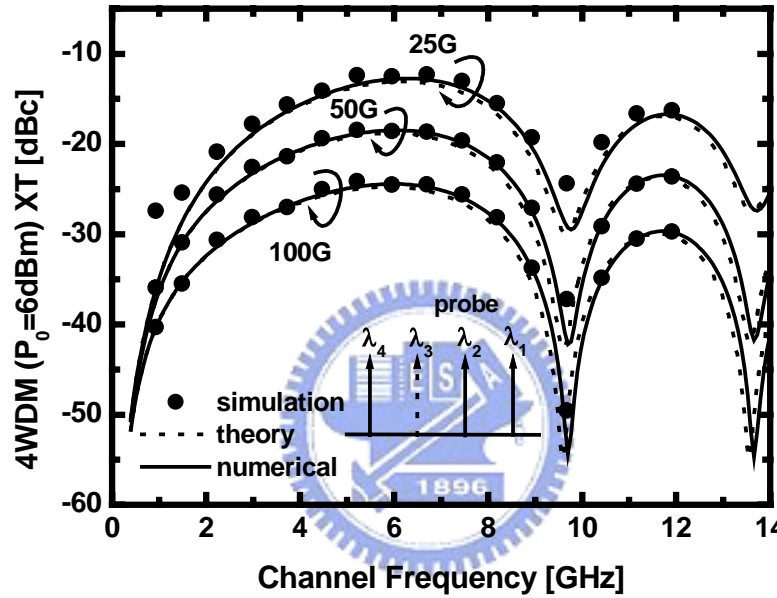


Fig. 2.9 Four wavelengths XT versus pump modulation frequency for wavelength separations of 25, 50 and 100 GHz (with the probe channel in the center (λ_3)). Circular, dotted and solid lines show the simulation, theoretical and numerical results, respectively. Three pump wavelengths are simultaneously modulated by three uncorrelated 64 QPSK channels (between 0.93 and 12.648 GHz) using USB/SCM. The average optical power per wavelength is 6 dBm.

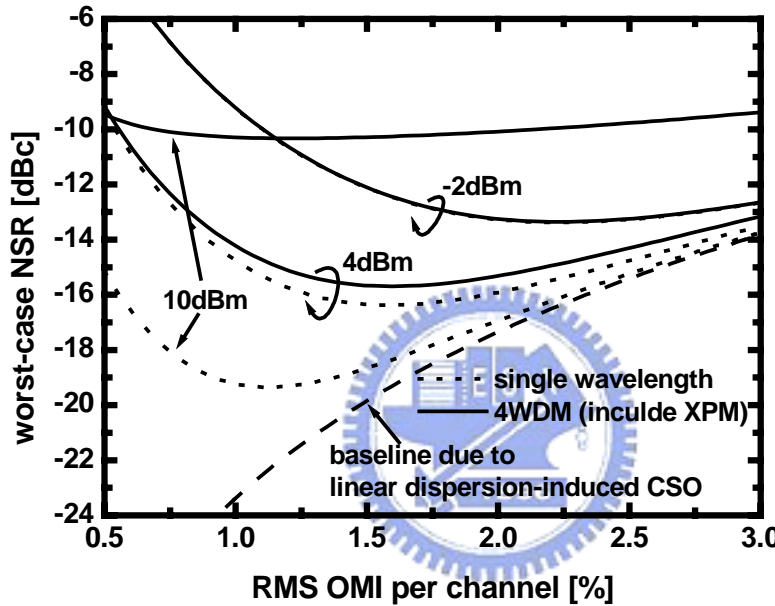


Fig. 2.10 Theoretical results of the worst channel NSR versus the $RMS\ OMI/ch$ for an average optical power per wavelength of -2, 4 and 10 dBm, for the system given in Table 2.3. Dotted lines are for single wavelength, while solid lines are for four wavelengths. The wavelength separation is 50 GHz. Dashed line is due to linear fiber dispersion-induced CSO.

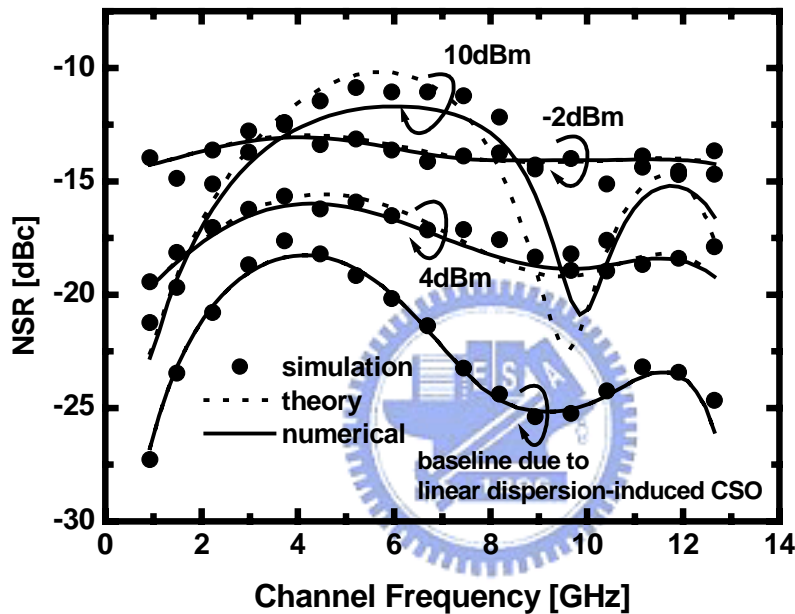


Fig. 2.11 NSR versus channel frequency in the case of four wavelengths for the system given in Table 2.3. Average optical power per wavelength is -2, 4 or 10 dBm. Circular symbols are simulation results; dotted lines are theoretical results; and solid lines are numerical results. The wavelength separation is 50 GHz and RMS OMNI per channel is 1.8%.

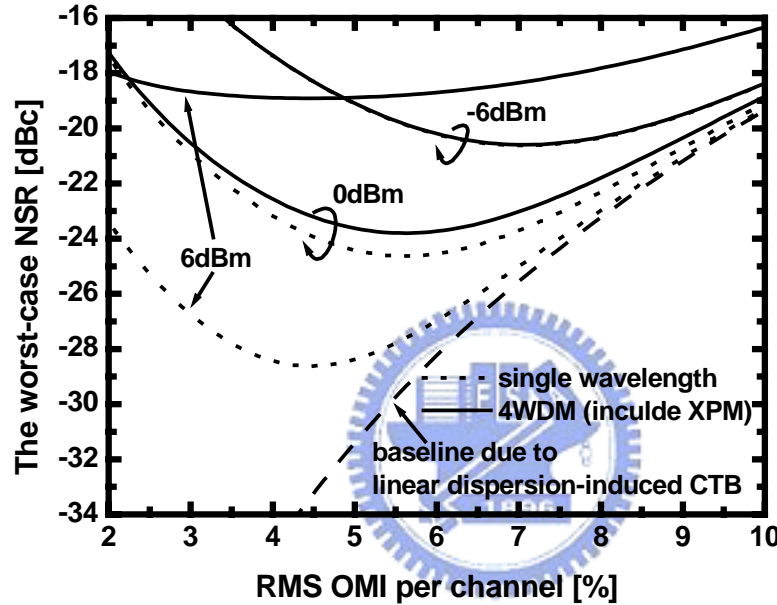


Fig. 2.12 Theoretical results of the worst channel NSR versus the *RMS OMI/ch* for an average optical power per wavelength of -6, 0 and 6 dBm.

Dotted lines are for the case of single wavelength, while solid lines are for the case of four wavelengths. The wavelength separation is 50 GHz. Dashed line is due to linear fiber dispersion-induced CTB.

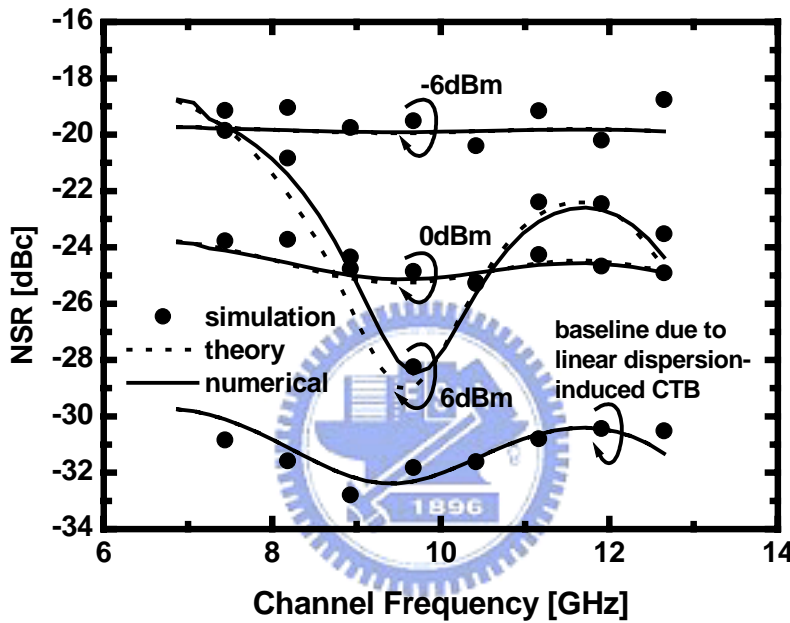


Fig. 2.13 NSR versus the channel frequency in the case of four wavelengths. Average optical power per wavelength is -6, 0 or 6 dBm. Circular symbols are simulation results; dotted lines are theoretical results; and solid lines are numerical results. The wavelength separation is 50 GHz and RMS OMI per channel is 5.5%.

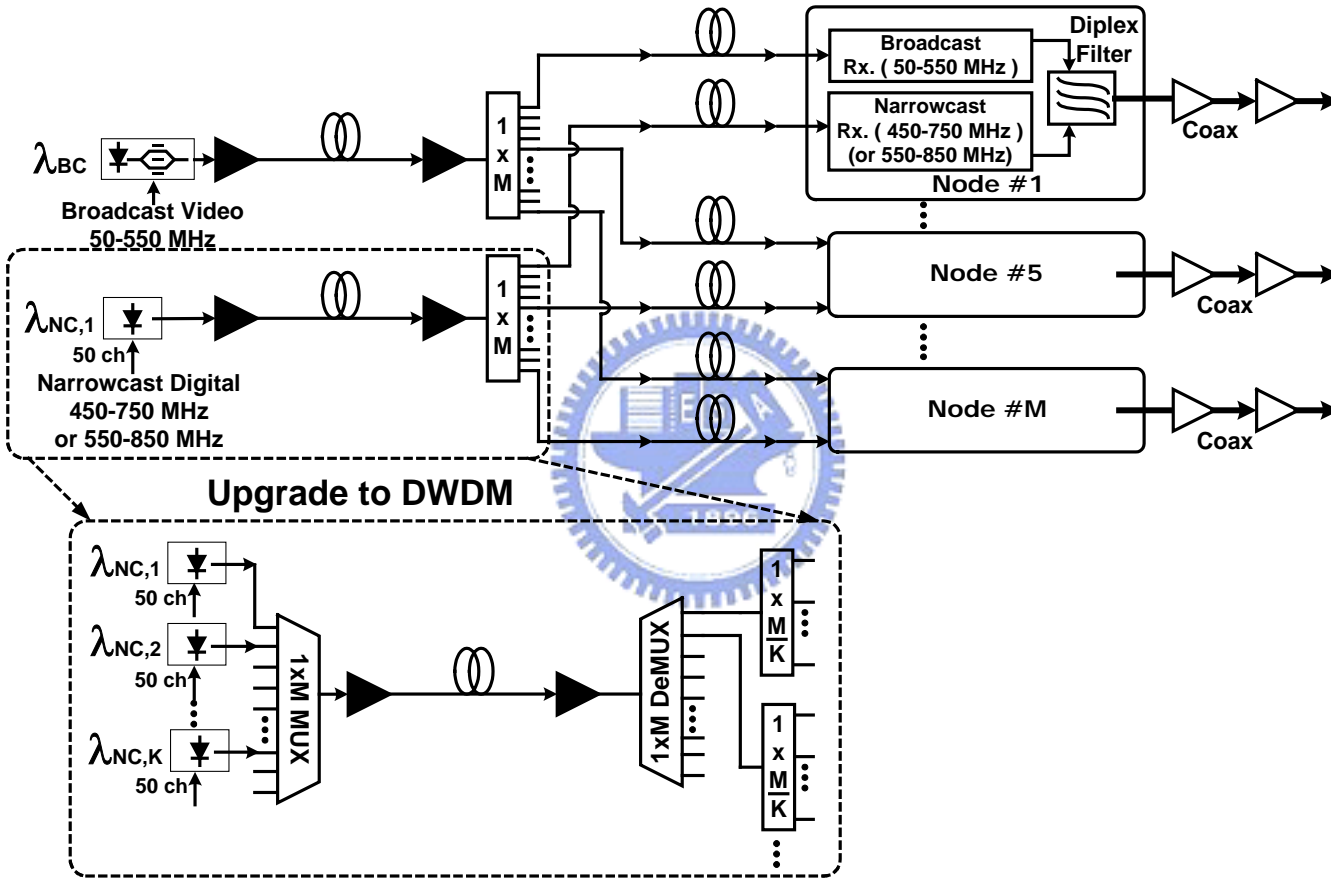


Fig. 3.1 Proposed HFC Network architecture for adding narrowcast services to broadcast services.

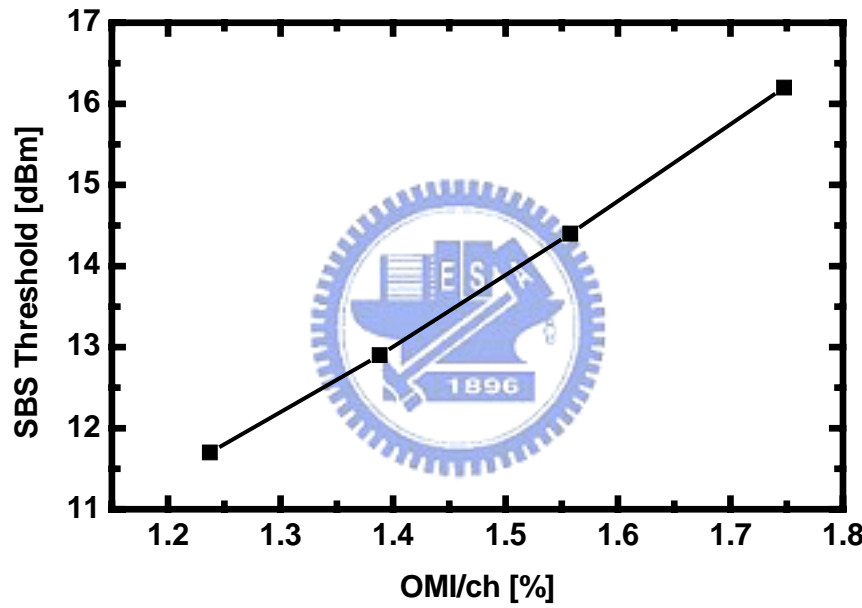


Fig. 3.2 Measured SBS threshold versus OMI/ch for 81 km conventional SMF.

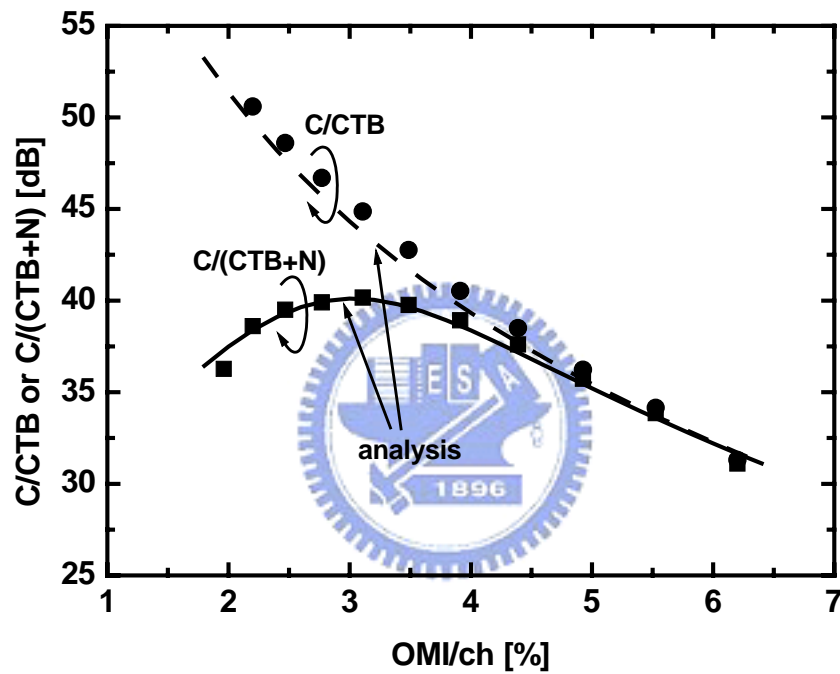


Fig. 3.3 Measured C/CTB (●) and C/(CTB+N) (■) of Ch.50 (centered@ $f = 745.25$ MHz, Bandwidth = 6 MHz) versus OMI/ch . Dashed and solid lines are analytical results.

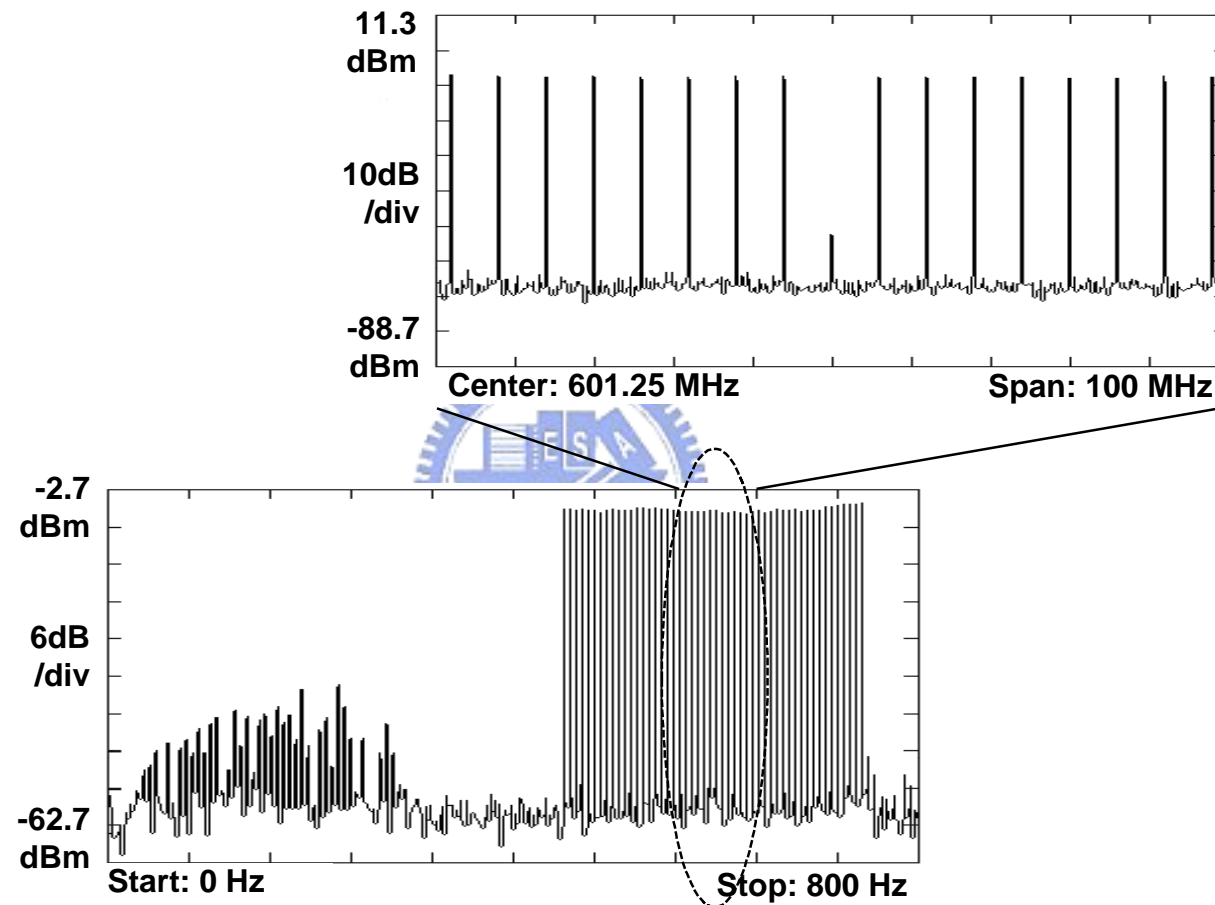


Fig. 3.4 Received RF spectrum after 102.5 km conventional SMF transmission and 14 dB splitting loss.

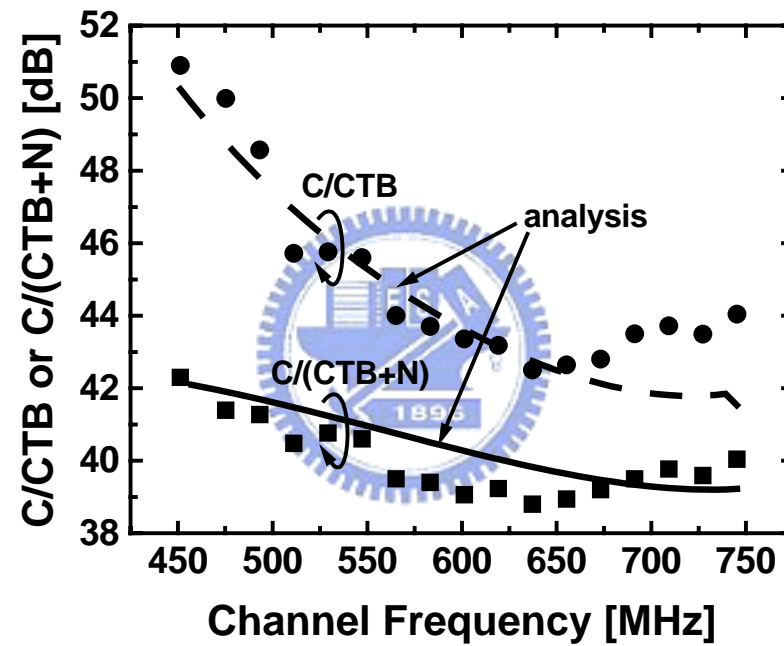


Fig. 3.5 C/CTB (●) and C/(CTB+N) (■) as a function of channel frequency. The dashed and solid lines are analytical results.

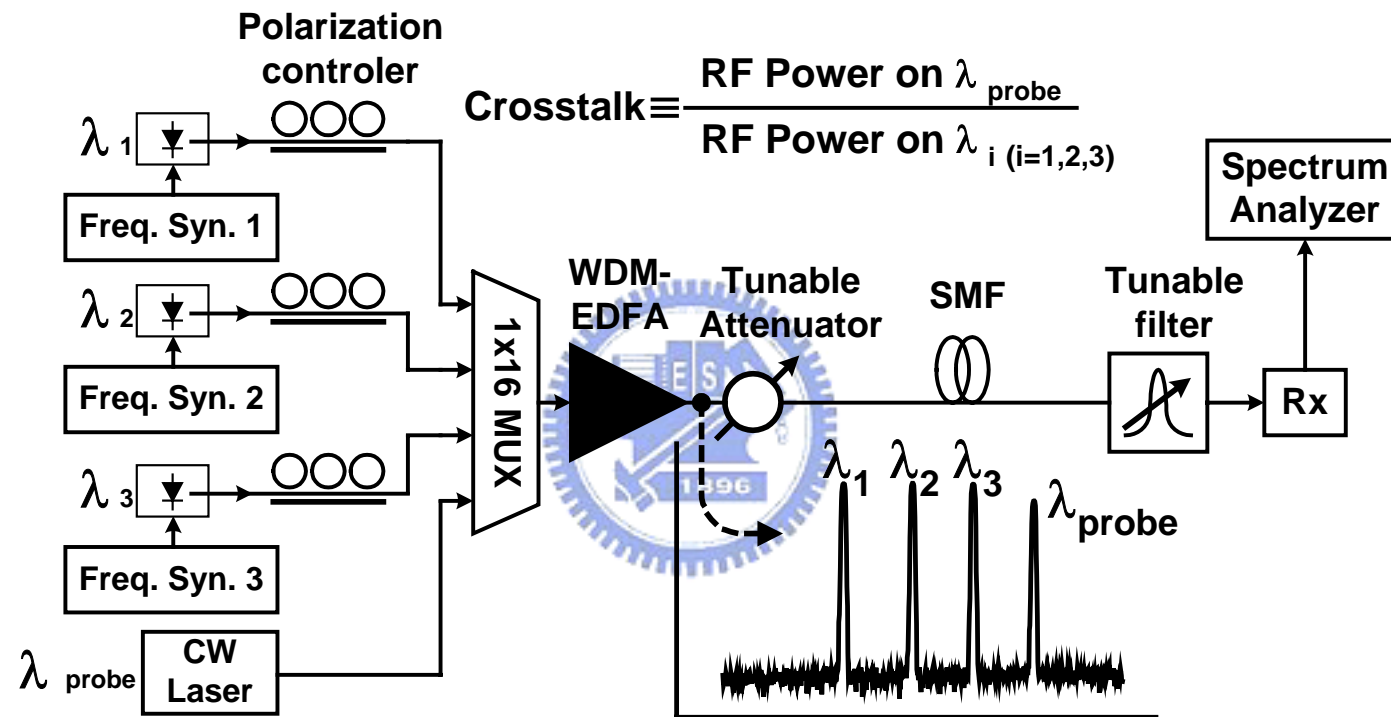


Fig. 3.6 4-wavelength experimental setup for measuring DWDM crosstalk. Wavelength spacing was 3.2 nm.

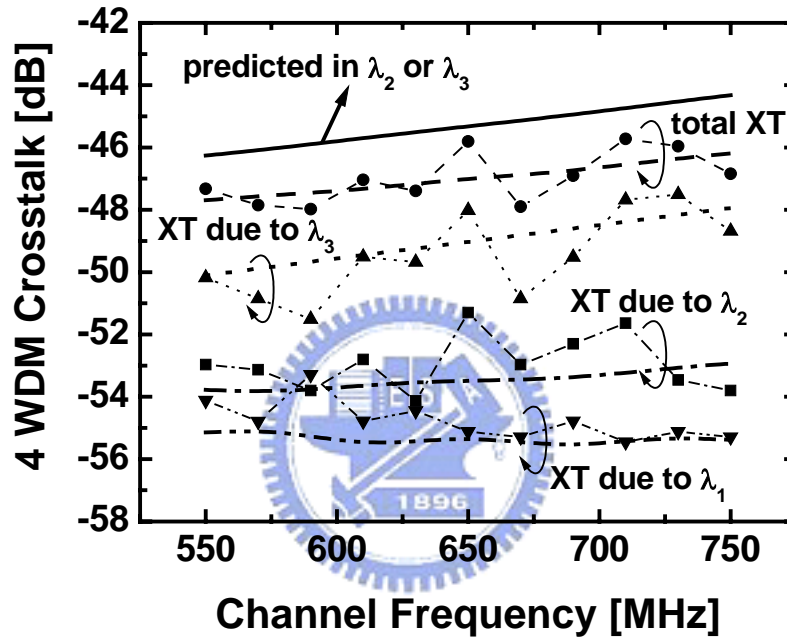


Fig. 3.7 Measured crosstalk in the probe wavelength due to λ_1 (\blacktriangledown), λ_2 (\blacksquare), λ_3 (\blacktriangle) and total crosstalk (\bullet) as a function of channel frequency. All broken lines are analytical results. Solid line is the predicted crosstalk at the middle (worst case) wavelength. Transmission distance is 80 km.

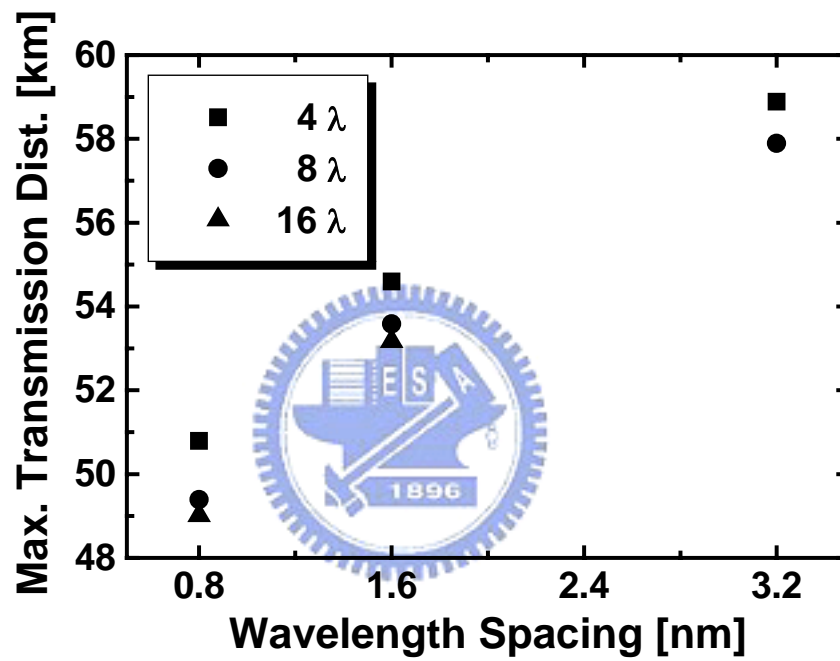


Fig. 3.8 Predicted maximum transmission distance between primary and secondary hub versus wavelength spacing for 4 (■), 8 (●) and 16 (▲) wavelengths. The transmission distance between secondary hub and optical nodes is fixed at 20 km.

Publication List

A. 期刊論文(journal papers)

1. W. H. Chen, J. K. Wong and Winston. I. Way, "An Evolutionary HFC Network Architecture for Adding Narrowcast Services," *J. Opt. Commun.*, vol. 22, pp. 74-77, March 2001.
2. W. H. Chen and Winston. I. Way, "Multi-Channel Single-Sideband SCM/DWDM Transmission System," *J. Lightwave Technol.*, vol. 22, no. 7, July 2004. (JLT #6532).

B. 研討會論文(conference papers)

1. Wei Hong Chen, MingChia Wu, Ching Ten Chang, Winston I. Way, "Self-phase-modulation-limited transmission distance of repeaterless 1.55 μ m multichannel AM-VSB external modulation systems," *Proceedings of SPIE*, pp. 138-145, Jun 1998.
2. W. H. Chen, J. K. Wong and W. I. Way, "Experimental Verification of an Evolutionary HFC Network Architecture for Adding Narrowcast Service," *OFC2000 Technical Digest*, pp. 157-159, paper WJ-5.

C. 專利(patents)

1. "An Optical Fiber Transmitter Using Chirped Fiber Grating and Pre-distortion Circuit For Long Distance Subcarrier Multiplexed Lightwave Systems," U.S. Patent No. 6,559,994, May 6, 2003.

簡 歷

姓 名 : 陳威宏

性 別 : 男

出生年月日 : 民國 62 年 1 月 25 日

籍 貫 : 嘉義縣民雄鄉豐收村好收 133-12 號

住 址 : 嘉義市民生南路 111 巷 13 號

電 話 : (05) 2283-528

Email : wei.cm87g@nctu.edu.tw



學 歷 : 國立交通大學電信工程研究所 博士

(87 年 9 月 ~ 93 年 7 月)

國立交通大學電信工程研究所 碩士

(85 年 9 月 ~ 87 年 9 月)

國立交通大學電信工程學系 學士

(81 年 9 月 ~ 85 年 9 月)